J. Mech. Phys. Solids 214 (2026) 106661

Contents lists available at ScienceDirect

Journal of the Mechanics and Physics of Solids

journal homepage: www.elsevier.com/locate/jmps

Dynamic control of rigidity via geometric frustration: Unifying central force network theory and responsive hyperelasticity for mechanical metamaterials

Santiago Gomez Melo [a,b], Falko Ziebert [a,b], Ulrich S. Schwarz [a,b,*]

[a] Institute for Theoretical Physics, Philosophenweg 19, Heidelberg, 69120, Germany
[b] BioQuant, Im Neuenheimer Feld 267, Heidelberg, 69120, Germany

ARTICLE INFO

Keywords:
Rigidity transition
Mechanical metamaterial
Geometric frustration
Second order rigidity
Morphoelasticity
Band structure

ABSTRACT

Recent advances in materials design and 4D-printing now allow one to realize programmable metamaterials that upon receiving a suitable stimulus dynamically change their effective macroscopic properties. For mechanical metamaterials, this has been demonstrated for example for the Poisson ratio and the strain-to-twist ratio. Variable stiffness has been so far only achieved for multiphase metamaterials with unit cells much larger than the millimeter scale. Here we suggest a design strategy that should work with one material and with unit cells on the micrometer scale. By combining central force network theory and responsive hyperelasticity, we show theoretically that one can dynamically control the shear modulus by programming geometric frustration into a stimuli-responsive pentamode structure. This phenomenon, known as geometric incompatibility, produces a rigidity phase transition in which the elastic modulus changes by several orders of magnitude. It results from inducing a state of self-stress that eliminates the floppy modes of the system by producing second order rigidity. The underlying physical principle seems to be at work in biological systems, for example in biopolymer networks and epithelial monolayers, but here it is predicted for entirely synthetic materials, like nematic elastomers and temperature-sensitive hydrogels, opening up the perspective of designing a new class of dynamic metamaterials.

1. Introduction

With the advent of micro- and nanofabrication technologies, in particular 3D-printing, the possibility of tailoring the macroscopic properties of a material in a bottom-up approach has become a reality, with far-reaching perspectives for the design of future materials of superior quality. In particular, the field of mechanical metamaterials aims to harness these technologies in order to produce new artificial structures with exotic mechanical properties beyond those of naturally occurring solids (Kadic et al., 2019). In order to do so, the design of mechanical metamaterials focuses on two main aspects: the geometry of the unit cell and the properties of its constituents. The exploration of intricate geometries in combination with carefully chosen constituents has opened the door to exciting possibilities such as metafluids with vanishing elastic moduli (Milton and Cherkaev, 1995; Kadic et al., 2012), mechanical material with memory (Sirote-Katz et al., 2024), topological insulators (Kane and Lubensky, 2013), realizations of odd elasticity (Scheibner et al., 2020) or negative index mechanical metamaterials (Nicolaou and Motter, 2012).

* Corresponding author.
E-mail address: schwarz@thphys.uni-heidelberg.de (U.S. Schwarz).

https://doi.org/10.1016/j.jmps.2026.106661
Received 5 December 2025; Received in revised form 12 April 2026; Accepted 29 April 2026
Available online 1 May 2026

The genesis of metamaterials came with an immense design space whose meaningful exploration remains a challenge, in spite of recent advances in computer-aided design involving machine learning, inverse problem strategies and topology optimization (Kadic et al., 2019; van Mastrigt et al., 2022; Zheng et al., 2023). Understanding the underlying mechanisms behind the desirable properties of a metamaterial may be used to identify physically motivated design principles with which one can tame the exploration of design space. Nature, and more specifically biology, can always serve as a source for such inspiration. Biological systems such as the cellular actin cytoskeleton, extracellular matrix, epithelial tissue monolayers and other molecular or cellular assemblies exhibit desirable characteristics for the next generation of mechanical metamaterials (Banerjee et al., 2020). They are capable of self-assembly into target shapes (Klein and Schwarz, 2014; Gomez Melo et al., 2023), shape shifts in response to external stimuli (Marée et al., 2012) and during development (Fuhrmann et al., 2024), rigidity transitions between a floppy and a rigid state (Petridou et al., 2021) and environment adaptability due to memory effects (Weichsel and Schwarz, 2010). These exciting properties respond to the demanding requirements of complex biological processes such as the embryo development (Petridou et al., 2021) and healing after wounding (Peña and Martin, 2024; Wool, 2008).

A common feature among biological systems is their ability to adapt to environmental cues. Stimuli-responsive materials are thus an attractive alternative to replicate the remarkable properties of living matter and extend 3D-printing into the time domain (4D-printing) (Momeni et al., 2017). Some prominent classes of such materials are liquid crystal elastomers (LCEs) and swelling hydrogels. The former are polymeric networks with embedded liquid crystal molecules exhibiting long range orientational order. Upon a temperature change the order is disrupted in the well known nematic-isotropic phase transition, which induces an anisotropic active strain under which the elastomer deforms (Warner and Terentjev, 2007). It has been shown that the deformation of the elastomer can be programmed by designing a specific nematic texture, which can be in turn controlled via electromagnetic fields (Münchinger et al., 2021) and scaffold confinement (Hsu et al., 2024). LCEs have been used to fabricate actuators with customized motion (Hsu et al., 2024; Kaczmarski et al., 2024) and even optomechanical metastructures capable of tuning their mechanical features (Münchinger et al., 2022). On the other hand, smart hydrogels can swell in solution when exposed to changes in temperature, pH and even magnetic fields. Consequently, this class of materials has shown to have wide range of applications including shape programmable materials, flexible electronics and mechanical actuators (Wang et al., 2024).

With biological inspiration in mind and the possibility of responsive metamaterials at hand, significant breakthroughs in the field of biomimetic materials and devices have been achieved. For example, exquisitely designed nematic textures in thin sheets of LCEs have been shown to buckle into intricate shapes like that of the human face (Aharoni et al., 2018), akin to the formation of target structures due to morphogen release during embryogenesis. Interestingly, shape programming via nematic order has also been experimentally achieved in cellular monolayers (Endresen et al., 2024), demonstraing the extent to which responsive materials can mimick living matter. Additionally, biomimetics has also impacted the field of soft robotics; biohybrid devices powered by living systems such as neuromuscular tissue or bacterial micromotors have been successfully fabricated and controlled with external optical or electrical signals (Appiah et al., 2019). Potential applications for these biodevices include robotic microsurgery and powered microactuators such as micropumps or microrotors (Appiah et al., 2019).

While many applications have been focused on programmable shape changes, it is equally interesting to also consider dynamical control of rigidity. Variable stiffness has been demonstrated before for mechanical metamaterial, but mainly for multiphase material, in which one material ensures the desired geometry, while the other can undergo some transition, for example a phase transition such as melting (Zheng et al., 2024; Rich et al., 2017), a jamming transition (Wang et al., 2019, 2021, 2025) or a glass transitions (Yuen et al., 2016; Chen et al., 2022). For the case of melting, it has been shown that the Young's modulus can be reduced by five orders of magnitude (Zheng et al., 2024). This dramatic change was possible due to the melting of a filler material confined by a solid matrix in the form of a triply periodic minimal surface that divides space into two interpenetrating labyrinths (Schwarz and Gompper, 1999). Jamming-based metamaterials, on the other hand, are compressed via pneumatic actuation, so that their underlying structure jams, thus increasing their modulus; such a strategy has been used in chain mail like interlocking structures (Wang et al., 2021), spherical packings (Wang et al., 2019) and silicone films (Wang et al., 2025). Finally, glass transitions have also been used to modify the stiffness of vitrifying binary polymer gels capable of liquid-liquid phase separation (Chen et al., 2022) and active fibers that combine thermoplastics with shape memory alloys (Yuen et al., 2016). These design strategies typically require large unit cells, ranging from the millimeter to the centimeter scales.

To dynamically control the rigidity of mechanical metamaterial, here we suggest an alternative strategy based on tunable prestress that should also work on the micrometer scale. It is inspired by the rigidity transitions observed in epithelial tissue monolayers and predicted by the vertex model (Hernandez et al., 2022), as well as in disordered network models for the actin cytoskeleton (Banerjee et al., 2020). Our strategy has several practical advantages compared to previous work on tunable moduli. First, it relies on a single responsive constituent capable of spontaneous contraction, such as an LCE or a hydrogel. This avoids the fabrication of interpenetrating multiphase metamaterials involving, for example, injection of a filler into a matrix (Zheng et al., 2024). Moreover, we explore the usage of hydrogels as possible constituents, which can be actuated via changes in pH and thus do not require any energy input from electric or heating elements (Yuen et al., 2016). Our blueprint is motivated by recent work with two-photon laser printing of LCEs (Hsu et al., 2024; Münchinger et al., 2022) and hydrogels (Tran et al., 2025), which can be implemented on the micrometer scale. Unifying central force network theory and responsive hyperelasticity, we combine the potentials of responsive constituents and tailored geometry to propose a blueprint of a single-phase metamaterial capable of a dynamic rigidity phase transition.

This work is structured as follows. First, we review the theory of rigidity in mechanical networks and from this derive a suggestion for a control strategy for a self-rigidifying structure. The proposal is then tested using finite element simulations for different values of geometric parameters of the structure and of the experimental parameters encoding the actuation. Finally, the underlying mechanism is analytically investigated via a variational ansatz. Our work expands upon the possibility of optomechanical and responsive

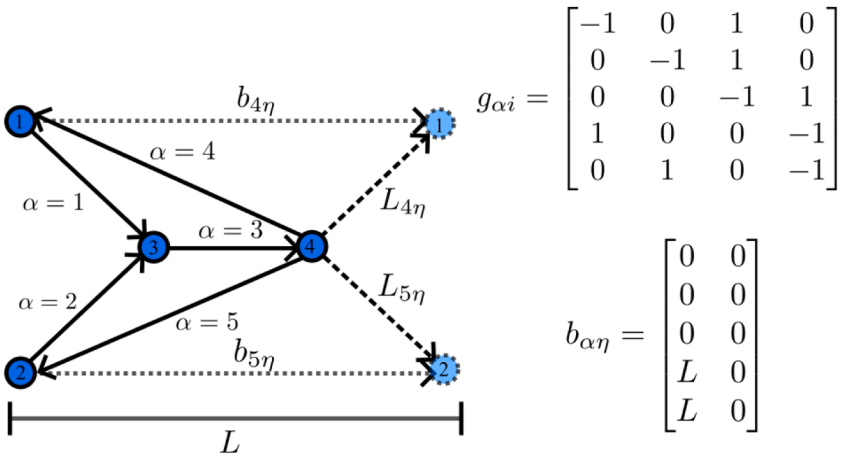

Fig. 1. Definition of a central force network for a two-dimensional graph with four nodes. The four nodes are indexed by subscript i and the five edges by subscript α, respectively. Connectivity is represented by the incidence matrix $g_{\alpha i}$. The graph is periodic in the horizontal direction, so the leftmost nodes (1 and 2) are connected to the rightmost nodes (4). The corresponding edge lengths are thus translated via a lattice vector $[L, 0]$, an operation encoded in the vector $b_{\alpha\eta}$, with η denoting the two space dimensions of this graph.

metamaterials by demonstrating that its actuation under additional constraints can drive the system to a prestressed state, known as a state of self-stress, that increases the shear modulus of the structure.

2. Methods

2.1. Theory of mechanical networks

We first review the well-known theory of central force networks, which explains rigidity transitions of first and second order (Hain et al., 2025; Merkel et al., 2019). A mechanical network is a graph in which nodes represent particles and edges represent non-zero interactions among these particles, which can be thought of as non linear springs. We consider a graph with N nodes connected by N_α edges, where the ith node has a coordinate $x_{i\eta}$ along direction η in d dimensions and edges are labeled by the subscript α. The connectivity of the graph, encoded in its incidence matrix $g_{\alpha i}$, relates the edge length vector $L_{\alpha\eta}$ to the node positions as (Hain et al., 2025)

$$L_{\alpha\eta} = \sum_i g_{\alpha i} x_{i\eta} + b_{\alpha\eta} \,, \tag{1}$$

where term $b_{\alpha\eta}$ encodes the boundary conditions of the network. The norm of the edge length is then $L_\alpha^2 = \sum_\eta L_{\alpha\eta}^2$. Eq. (1) is sufficient to introduce the notions of floppy and rigid networks. A network is called *floppy* if there exists a non-trivial dN dimensional parametric curve $x_{i\eta} = x_{i\eta}(t)$ over which the edge lengths L_α remain constant. By non-trivial we exclude isometric, or distance preserving, maps such as rigid movements. If only trivial motions leave the edge lengths constant, then the network is said to be *rigid* (Connelly and Servatius, 1994). The definitions used in Eq. (1) are illustrated for a simple two-dimensional graph with four nodes in Fig. 1.

Although not necessarily required for rigidity theory, is natural in our context to assign a potential function U_α to each edge. It is taken to be a lower bounded and coercive (i.e. $U_\alpha \to \infty$ as $L_\alpha \to \infty$) central potential depending only on the length of the edge L_α. This guarantees that all U_α have a global minimum, and so does the total mechanical energy $E(\{x_{i\eta}\}) = \sum_\alpha U_\alpha(L_\alpha)$. The most relevant quantities in central network theory, which help determine whether a network is rigid or not, can be extracted from the Taylor expansion of the energy function E up to second order (Connelly and Servatius, 1994)

$$E \approx \sum_\alpha U'_\alpha \underbrace{\partial_{i\eta} L_\alpha}_{R_{\alpha i\eta}} x_{i\eta} + \frac{1}{2}\Big[U''_\alpha (\partial_{i\eta} L_\alpha)(\partial_{j\kappa} L_\alpha) + \underbrace{U'_\alpha \partial^2_{i\eta,j\kappa} L_\alpha}_{P_{\alpha i\eta j\kappa}}\Big] x_{i\eta} x_{j\kappa} \,, \tag{2}$$

where we have defined the *rigidity matrix* $R_{\alpha i\eta}$ and the *prestress stability matrix* $P_{\alpha i\eta j\kappa}$. By direct computation, these can be written in terms of the edge length vectors $L_{\alpha\eta}$, their length L_α and the incidence matrix $g_{i\alpha}$ as

$$R_{\alpha i\eta} = \frac{L_{\alpha\eta}}{L_\alpha} g_{\alpha i}, \; P_{\alpha i\eta j\kappa} = \frac{U'(L_\alpha)}{L_\alpha}\Big(g_{\alpha i} g_{\alpha j}\delta_{\eta\kappa} - R_{\alpha i\eta} R_{\alpha j\kappa}\Big) \,. \tag{3}$$

The rigidity matrix encodes an infinitesimal response in edge lengths resulting from an infinitesimal node displacement. It is clear that the edge lengths L_α will remain unchanged upon an infinitesimal transformation $x_{i\eta} \to x_{i\eta} + \epsilon v_{i\eta}$ if $v \in \ker(R)$. The vectors belonging to $\ker(R)$ are therefore known as *linear zero modes* (LZM) or first order flexes. Since rigid motions obviously fulfill this

condition, they are known as trivial zero modes. If no non-trivial linear zero mode exists, then the system is said to be *first order rigid*. It has been shown that if a network is first order rigid, then it is rigid in the above defined sense (Connelly and Servatius, 1994).

Mechanical equilibrium requires that N_α-tuples composed of edge tensions U'_α lie in the left hand side kernel $\ker(R^T)$; states in this space with non zero tension $U'_\alpha \neq 0$ for at least one edge α_0 are known as *states of self stress* (SSS). From the dimension of $\ker(R)$ and $\ker(R^T)$, Maxwell and Calladine derived an equation that determines if a system is first order rigid based on the difference between the number of edges N_α and the number of degrees of freedom dN (Maxwell, 1864; Calladine, 1978). The Maxwell-Calladine constraint count condition is a consequence of the rank-nullity theorem applied to the mappings R and R^T and the fact that the rank of these two operators match,

$$\begin{aligned} \operatorname{rank} R = \operatorname{rank} R^T &\implies \dim R - \operatorname{null} R = \dim R^T - \operatorname{null} R^T \\ &\implies dN - N_\alpha = N_{LZM} - N_{SSS}, \end{aligned} \tag{4}$$

where $N_{LZM} = \operatorname{null}(R)$ is the nullity of R, which counts the number of LZMs, and $N_{SSS} = \operatorname{null}(R^T)$ is the nullity of R^T, which counts the number of SSSs. The condition imposed by Eq. (4) allows for the distinction between an *underconstrained* network, with $dN > N_\alpha$; *overconstrained* network, with $dN < N_\alpha$; and a *critically constrained* network with $dN = N_\alpha$. This distinction is the mechanism behind rigidity transitions due to jamming, in which the number of constraints are increased until all non-trivial linear zero modes are eliminated and the network becomes rigid.

Underconstrained networks of constant connectivity, which have constant number of degrees of freedom and constraints, can still be rigid if their prestress stability matrix P is positive definite in the space of non trivial linear zero modes (Hain et al., 2025; Connelly and Servatius, 1994; Gortler et al., 2025); note that this is only possible for prestressed states with non zero edge tensions U'_α, i.e. states of self stress. It is in fact simple to show, see Appendix A, that if a graph with a single connected subgraph (i.e. there are no disjoint networks) has all edges under tension (i.e. $U'(L_\alpha) > 0$), then P is positive definite in such subspace. The fact that a state of self-stress induces a non-zero energy penalty for all LZMs at the second order is the key element for rigidity transitions due to *geometric incompatibility*.

Geometric incompatibility refers to the impossibility of a mechanical network to attain the minimum configuration of all its individual elements when exposed to additional geometrical restriction. Suppose that the space of allowed edge lengths is given by $\Omega \subseteq \mathbb{R}^{N_\alpha}$. We then say that the mechanical network is geometrically incompatible if the system of possibly nonlinear equations $U'(L_\alpha) = 0$ has no solution in Ω. If a system exhibits geometric incompatibility, then clearly all of its equilibrium points will be states of self-stress.

Two simple examples help illustrate the concept of geometric incompatibility. The first one is a chain of n springs in 2D with its two ends fixed at positions (0,0) and (a,0). Then

$$\Omega = \Big\{ L_\alpha \Big| \sum_\alpha L_{\alpha x} = a \Big\}. \tag{5}$$

If each spring has a rest length l_0, then the system can only attain $L_\alpha = l_0$ if $nl_0 \geq a$, so the chain can bend in the transverse direction at no energy cost. Otherwise, the system becomes geometrically incompatible, and so chain straightens and transverse displacements are now energetically costly. This is the mechanism behind the tensing of a string.

The second, more interesting example is found in the modelling of epithelial monolayer sheets and foams. These are modelled as an infinite tiling of polygons with an energy function given by the vertex model (Farhadifar et al., 2007):

$$E = \frac{1}{2} \sum_i k_A (A_i - A_0)^2 + k_p (P_i - P_0)^2, \tag{6}$$

where i runs over all polygons, A_i and P_i are the area and perimeter of the ith polygon, k_a and k_p are rigidity coefficients, and A_0 and P_0 are a preferred area and perimeter. Geometric incompatibility manifests itself via the isoperimetric inequality; the ratio A/P^2 of an n sided polygon is always bounded above by that of a regular polygon with n sides. Hence,

$$\Omega = \Big\{ (A_i, P_i) \Big| \frac{A_i}{P_i^2} \leq \frac{n}{4} \cot \frac{\pi}{n} \Big\}. \tag{7}$$

Polygons can attain their individual rest configuration $A_i = A_0$ and $P_i = P_0$ only if $A_0/P_0^2 \leq \frac{n}{4} \cot \frac{\pi}{n}$, which leads to a mechanically compliant state (Hernandez et al., 2022). On the other hand, $A_0/P_0^2 > \frac{n}{4} \cot \frac{\pi}{n}$ leads to geometric incompatibility and thus to a rigid system.

2.2. Elastic moduli of mechanical networks

The second rigidity transition manifests itself in the static mechanical moduli of the network, defined as the change in the minimized energy of the structure upon a prescribed infinitesimal deformation $x_{i\eta} \to \gamma A_{\nu\eta} x_\eta$ with intensity γ or an equivalent probing force field $\vec{f} = \sigma \hat{f}$ with intensity σ:

$$\mu \equiv V \left(\frac{d^2 E_{\min}}{d\sigma^2} \right)^{-1}_{\sigma=0} = \frac{1}{V} \left(\frac{d^2 E_{\min}}{d\gamma^2} \right)_{\gamma=0}, \tag{8}$$

where V is the volume occupied by the network and $E_{\min}(\vec{f}) = E(x^*_{i\eta}(\vec{f}), \vec{f})$ corresponds to the minimized energy at equilibrium positions $x^*_{i\eta}$ as a function of the probe $\vec{f}$. This quantity relates to the eigenvalues ω_k^2 and orthonormal eigenvectors $\hat{u}_k$ of the Hessian

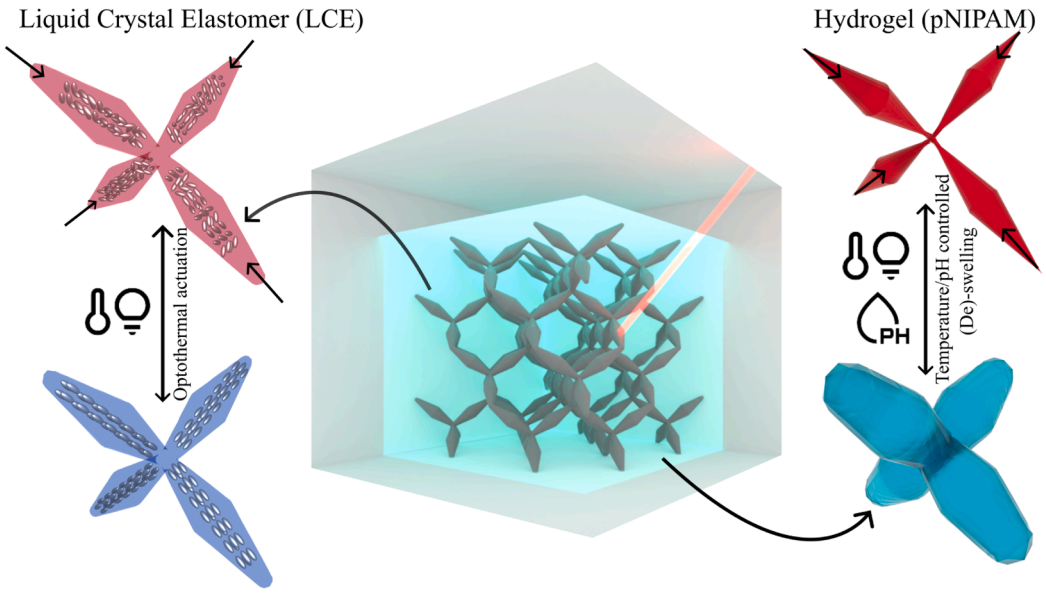

Fig. 2. A pentamode metamaterial cube is fabricated from a responsive constituent and then actuated via an external control while keeping the outermost planes, depicted in turquoise, at a fixed position (zero displacement boundary conditions). The actuation generates a contractile strain on the bars, but the contraction is precluded by the fixed planes. This induces a state of geometric frustration where the tension in the edges rigidify the system in a similar way as a string becomes tense when stretched beyond its natural length. We propose two possible constituents for the metamaterial's realization: a liquid crystal elastomer (LCE) with a piecewise constant nematic director parallel to the direction of each bar and a swelling hydrogel like pNIPAM.

$H = \partial^2_{i\eta,j\kappa} E$ as

$$\mu = \begin{cases} 0 & \text{proj}_{\ker(H)} f \neq 0 \\ \frac{a^3}{2}\left(\sum_{k|\omega_k\neq 0} \frac{\langle \hat{u}_k \cdot \hat{f}\rangle^2}{\omega_k^2}\right)^{-1} & \text{otherwise,} \end{cases} \tag{9}$$

where a is the length of the unit cell. The first case indicates that a force with a non zero projection onto the kernel of the Hessian cannot be counteracted by the network. Additionally, the eigenvalues ω_k are proven to increase with increasing tension U'_α. This is the essence of the mechanism behind the variable modulus, as an increase in ω_k will lead to an increase in μ. Details of these derivations regarding elastic moduli of mechanical networks may be found in Appendix B.

In view of the aforementioned theory, we reason that a metamaterial based on an underconstrained network made of a constituent capable of spontaneously contracting under an external stimulus should rigidify if an additional constraint precludes the contraction from occurring, thus generating the desired state of prestress. As the base structure, we choose the well known pentamode proposed by Milton and Cherkaev (Milton and Cherkaev, 1995; Kadic et al., 2012) and shown in Fig. 2. Since the pentamode has the same structure and connectivity as a diamond lattice, it is severely underconstrained, because each node has four neighbours in three dimensions, so Maxwell-Calladine constraint counting reads $3N - 4N/2 = N > 0$ for N nodes. This is consistent with its vanishing elastic moduli. If such a material is actuated such that the edges contract, but the outermost nodes are held fixed (compare Fig. 2), the system will not be able to relax and tensile prestress emerges, akin to nonzero edge tensions U' in states of self stress. The presence of prestress should therefore rigidify the pentamode according to the theory of mechanical networks. Furthermore, stronger actuation will generate stronger prestress and thus a larger elastic modulus.

2.3. Continuum theory for responsive elastic media

We next explore the use of two possible constituents capable of contracting: an LCE with an appropriately chosen nematic director, which contracts upon heating, and a hydrogel, capable of de-swelling due to solvent desorption upon pH or temperature changes. Given that these materials are capable of large and spontaneous deformations, the appropriate theory describing these two is non-linear morphoelasticity. In this formalism, the spontaneous anisotropic deformation of a LCE upon a temperature change from the rearrangement of the LC mesogens is modelled via the growth tensor formalism (Mihai and Goriely, 2021; Goriely, 2017). If $\hat{v}(x)$ is the nematic orientation field, then the growth tensor G is given by

$$G(\lambda) = (\lambda - \lambda^{-\frac{1}{2}})\hat{v} \otimes \hat{v} + \lambda^{-\frac{1}{2}} I, \tag{10}$$

where I is the identity tensor and λ is a stretch ratio which acts as a control parameter that can be experimentally tuned through temperature (Münchinger et al., 2021; Hsu et al., 2024). The growth tensor in Eq. (10) essentially states that when the LCE is

actuated, it will locally stretch by a factor λ along the direction $\hat{v}$ and shrink by a factor $\lambda^{-1/2}$ in the plane orthogonal to $\hat{v}$. Observe that the unactuated state corresponds to $\lambda = 1 \implies G = I$. The neoHookean strain energy density function w with a growth tensor decomposition is then given by

$$w(F,p) = \frac{\mu_c}{2}\mathrm{Tr}[G^{-1}FF^T(G^T)^{-1}] - p(\det F - 1), \tag{11}$$

where μ_c is the shear modulus of the constituent material, $F = I + \nabla\vec{u}$ is the deformation gradient associated with a displacement field $\vec{u}$ and p is a Lagrange multiplier locally enforcing incompressibility. For our proposed metamaterial, the nematic director $\hat{v}$ is aligned with the axis of each bar $\hat{n}$, so that $\hat{v} = \hat{n}$.

On the other hand, the swelling of a hydrogel due to solvent absorption is represented through its swelling fraction ϕ. This parameter encodes the percentage volume change due to solvent absorption. For example, $\phi = 1.5$ means that the hydrogel will increase its volume by 50 %. If the hydrogel is perfectly incompressible, ϕ fixes the determinant of the deformation tensor (Webber and Worster, 2023), $\det(F) = \phi$. In this case, the strain energy density is given by

$$w(F,p) = \frac{\mu_c\phi^{-2/3}}{2}\mathrm{Tr}[FF^T] - p(\det F - \phi), \tag{12}$$

where the factor $\phi^{-2/3}$ in the first term ensures consistency with a compressive neoHookean model in the limit of infinite compressibility modulus. As in the case of the LCE, ϕ can be experimentally controlled via temperature or pH. The total energy E is then the integral over the material body volume of w, i.e. $E = \int w dv$. In order to generate geometric incompatibility, we consider the nodes at the outermost faces of a cube to have zero displacement. This can be achieved, for instance, by joining each node at opposing faces with rigid bars, thus introducing non-local interactions (Chen et al., 2023). Such realization would mainly constrain the nodes in the direction perpendicular to their respective plane, while still allowing for motion parallel to it, which is required for a shear experiment.

The solution to the hyperelastic equations may be analytically approximated by means of a variational ansatz, which coarse-grains the infinite degrees of freedom of each bar into a single valued energy function. We treat the case of a LCE and a hydrogel separately. For the former case, a suitable ansatz for the deformed configuration of each bar is given by $\vec{x} = F\vec{X}$ with

$$F = (\beta - \beta^{-\frac{1}{2}})\hat{n}\otimes\hat{n} + \beta^{-\frac{1}{2}}I, \tag{13}$$

for some unknown parameter β. Such solution supposes that the bar will stretch uniaxially along its axis by a factor β and contract in the orthogonal plane by $\beta^{-\frac{1}{2}}$ so that incompressibility is fulfilled. Inserting this ansatz into Eq. (11), the total energy of the αth bar then reads

$$E_\alpha(\beta_\alpha,\lambda) = \overbrace{\frac{\mu_c V_b}{2}}^{c}\left(\frac{2\lambda}{\beta_\alpha} + \frac{\beta_\alpha^2}{\lambda^2}\right), \tag{14}$$

where V_b is the volume of the bar and the quantity $c = \mu_c V_b$ acts as a spring constant with dimensions of energy. This expression has a minimum at $\beta^* = \lambda$ implying that the deformed length $l = \lambda L_0$, so that the rest configuration is simply a stretched bar by a factor λ.

For the case of hydrogels, the zero displacement boundary conditions constrain the deformation of the bars along their axis, but not perpendicularly. Therefore, a reasonable ansatz would take the swelling of the hydrogel to be exclusively perpendicular to the axis of each bar,

$$F = \left[\beta - \left(\frac{\phi}{\beta}\right)^{\frac{1}{2}}\right]\hat{n}\otimes\hat{n} + \left(\frac{\phi}{\beta}\right)^{\frac{1}{2}}I, \tag{15}$$

where now the coarse-grained energy of the ith bar reads

$$E_\alpha(\beta_\alpha,\phi) = \frac{c\phi^{-2/3}}{2}\left(\frac{2\phi}{\beta_\alpha} + \beta_\alpha^2\right), \tag{16}$$

with a minimum at $\beta^* = \phi^{1/3}$.

The variational principle requires that the energy function $E_{tot} = \sum_\alpha E_\alpha(\beta_\alpha)$ be minimized with respect to all free parameters β_α. Hence, the coarse-graining procedure has reduced the problem to that of a central force mechanical network with an energy functional given by Eq. (14) for the case of LCEs and by Eq. (16) for the case of a hydrogel. Consequently, a rigidity transition is expected from a responsive pentamode; actuation with $\lambda, \phi < 1$ will force the bars to contract due to their new shrinked rest configuration. However, such contraction is precluded if the metamaterial has fixed outermost nodes, thus forcing the structure into a frustrated state of self stress where the bars are under tension. This desired tensile prestress will stabilize the soft modes of the otherwise unactuated structure and so the system will rigidify, akin to the emergent rigidity of a tensed string or vertex model.

3. Results

3.1. Numerical results with the finite element method

To demonstrate that a pentamode can be rigidified by geometric incompatibility, we defined pentamode nodes as shown in Fig. 3(a) and simulated a cube of the metamaterial as shown in Fig. 3(b). The suggested material could be made of incompressible

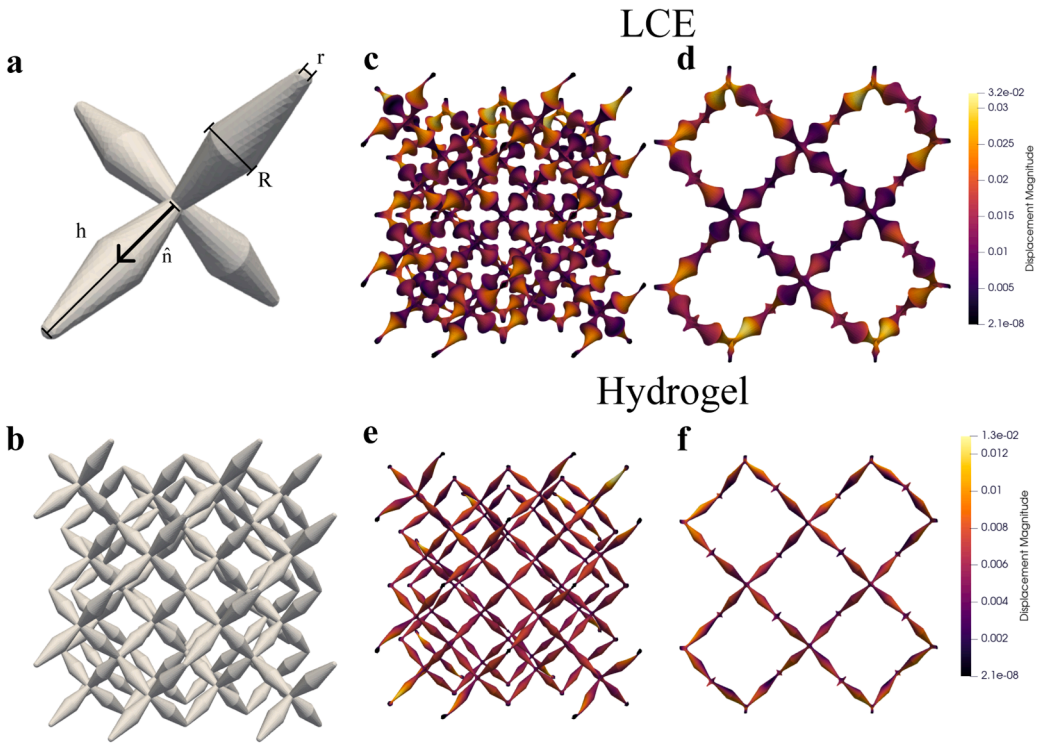

Fig. 3. (a) A single lattice site of the pentamode metamaterial consists of four bars with height h, node radius r and waist radius R. The axis of each bar is represented by the unit vector $\hat{n}$. For all simulations, $h = 1$, $r = 0.05$ and R was varied between $3r$ and $5r$. All bars are at an angle of 109.5° with respect to each other, the same as for carbon bonds in diamond. (b) The unactuated state of the simulated pentamode is a collection of conical bars arranged in a diamond crystal lattice. (c-f) Deformed configuration of the actuated pentamode made from a LCE (c), sliced along the midplane (d), and a hydrogel (e), sliced along the midplane (f), for a control parameter of $\lambda = \phi = 0.9$. In (c-f) the actuation is magnified by a factor of 10 for clarity and the coloring corresponds to the magnitude of the displacement field, normalized so that the bars have a length of 1. In both cases the largest displacements are observed in the outermost bars of the structure, whereas the innermost edges experience a significantly lower displacement.

swelling hydrogels or liquid crystal elastomers, compare Fig. 2. Their elastic energy density functions are given by Eqs. (12) and (11), respectively. We simulated their actuation using the Finite Element Method (FEM) implemented with the open source package FEniCSx (Baratta et al., 2023). Structures with different values of the waist radius R were tested, while keeping the beam's rest length $h = 1$ and the nodes radius $r = 0.05$ constant. These geometric variables are depicted in Fig. 3(a). In both cases the energy functional is minimized for several values of their respective control parameters (λ or ϕ) and different values of the ratio between smaller and bigger radii R/r. In all cases the Dirichlet boundary condition $\vec{u} = \vec{0}$ is imposed at the outermost nodes on all sides of the cube. Finally, the shear modulus of the actuated structure can then be computed by imposing a shear displacement boundary condition $u_i = \gamma \sum_j \delta_{i1}\delta_{j2}x_j$ with shear ratio $\gamma = 0.005$ on all sides of the previously deformed structure. The structure is then allowed to relax to a new energy minimum from which the shear modulus μ is read as

$$\mu = \frac{1}{V}\frac{d^2E_{\min}}{d\gamma^2} \approx \frac{E_{\min}(\gamma) - 2E_{\min}(0) + E_{\min}(-\gamma)}{V\gamma^2}, \tag{17}$$

where V is the volume of the cube in which the structure is contained and $E^*(\gamma)$ is the minimized energy as a function of the shearing ratio γ,

$$E_{\min}(\gamma) = \min_{(\vec{u},p)} \int w dx \text{ s.t. } u_i|_x = \sum_j \gamma\delta_{i1}\delta_{j2}x_j = \sum_j \gamma\delta_{i1}\delta_{j2}X_j, \tag{18}$$

where $u_i|_x$ being the displacement field at the outermost nodes of the cube, X_j is the unactuated, or material, position vector component and x_j is the actuated, or deformed, position vector. We note that $x_j = X_j$ in the outermost nodes because of the zero boundary conditions of the actuation.

In Fig. 3(c)–(f) we display the deformed configuration for a pentamode with an LCE and a hydrogel. We plot the displacement field mangitude $\vec{u} = \vec{x} - \vec{X}$ stemming from the difference between the unactuated and the actuated state. In both cases we observe that the bars respond mostly radially, with little change in their length. This qualitatively matches the piecewise constant ansatz from Eqs. (14) and (16). Furthermore, the displacement in the bars closest to the boundary show larger magnitudes compared to their inner counterparts, as depicted in the slices in Fig. 3(d) and (f). Because the lengths of the bars are different from their minimum energy

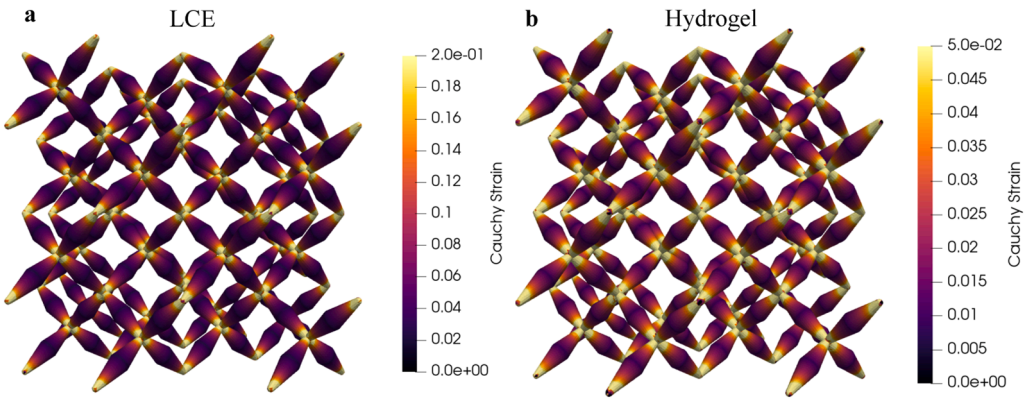

Fig. 4. Cauchy strain tensor, defined in Eq. (19), contracted with the unit vector $\hat{n}$ parallel to the axis of symmetry of each bar $\sum_{ij} C_{ij} n_i n_j$ for the case of a LCE with $\lambda = 0.9$(a) and a hydrogel with $\phi = 0.9$(b). In both cases the strain concentrates at the nodes, where the tension of the four adjacent bars must cancel in order to sustain mechanical equilibrium. In contrast, the center of the bars experience negligible strain.

value, they should experience a non-zero strain which generates the state of self-stress. This is confirmed by the left Green-Cauchy strain tensor C,

$$C = \begin{cases} \frac{1}{2}(F^T (G^{-1})^T G^{-1} F - I) & \text{for a LCE} \\ \frac{1}{2}(\phi^{-2/3} F^T F - I) & \text{for a Hydrogel} \end{cases} \tag{19}$$

This strain measure is different from the normal right Cauchy-Green strain tensor $C = \frac{1}{2}(F^T F - I)$ because the energy functional is minimal for $F^T F = G^T G$ rather than $F^T F = I$ in the case of LCEs. For hydrogels, the extra factor of $\phi^{-2/3}$ decouples the volumetric effects so that the tensor is purely deviatoric.

In Fig. 4, we plot the contraction $C_{nn} = \sum_{ij} C_{ij} \hat{n}_i \hat{n}_j$ corresponding to the component of the strain tensor in the direction of the beam's axis $\hat{n}$. In both cases it is clear that C_{nn} is always positive, indicating that all beams are under tension and thus confirming the state of self-stress due to geometric incompatibility. In particular, the highest values for the Cauchy strain component are observed near the nodes, which is expected since it is at the nodes where the tensions of the four neighbouring beams must balance in order to fulfill mechanical equilibrium. Finally, some discontinuities for the tensor component arise at the center of the nodes. This is understandable since $\hat{n}$ is ill-defined at the node center. While C_{nn} is an unusual strain measure, the analysis remains valid for other standard metrics such as the Frobenius norm of the left Green-Cauchy strain tensor C from Eq. (19), also known as equivalent strain. This is reported in Appendix C.

The shear modulus of the metamaterial μ is plotted as a function of the control parameter and the radii ratio R/r in Fig. 5(a) for the case of a LCE and in Fig. 5(b) for the case of a hydrogel, respectively. It is first clear that for both constituents the shear modulus decreases with increasing R/r regardless of the control parameter. Such behavior is consistent with that found for an unresponsive pentamode composed of a linear elastic material, for which a scaling law $\mu \sim R^\beta$ with $\beta \sim 1.3$ was reported (Kadic et al., 2012). It follows that $\mu a^3/c \sim R^{\beta-2}$ because $c = \mu_c V \sim hR^2$. The scaling of μ with the radii ratio occurs because r controls the bending rigidity at the nodes, which is the main contribution to the finite value of μ; for the idealized case of $r \to 0$, the original design by Milton and Cherkaev (Milton and Cherkaev, 1995), there is no bending rigidity and so $\mu = 0$ exactly.

In addition to the radii ratio R/r, Fig. 5 shows that the control parameter has a dramatic impact on the shear modulus μ and therefore be used to tune it externally; for the lowest values of the control parameter of 0.6, the metamaterial's shear modulus takes its highest values of $\sim 10\mu_c V/a^3$ for a LCE and $\sim 5\mu_c V/a^3$ for a hydrogel. As the control parameter is driven closer to unity, the shearing modulus drops by around two orders of mangitude in both cases, reaching values as low as $\sim 0.08\mu_c V/a^3$ for both constituents when the control parameter is above 1. Such behavior, reminiscent of a second phase transition, is the hallmark of a rigidity transition (Merkel et al., 2019) driven by geometric incompatibility, as demonstrated by the positive Cauchy strain shown in Fig. 3. This confirms that a state of self-stress can be attained by a responsive constituent exposed to geometric constraints, resulting in the overall ridification of the metamaterial.

There exist two competing effects that affect the overall rigidity of the structure: the shrinkage of the bars near the nodes, seen in Fig. 3, and the build-up of stress, seen in Fig. 4. As discussed, the former is expected to reduce the modulus, while the latter tends to increase it. The results of the shear modulus in Fig. 5 suggest that the prestress overcomes the size reduction of the bars. This is expected because of the incompressibility requirement; for a LCE, the incompressibility of the nodes, in combination with the fact that the growth tensor in Eq. (10) is isochoric, limits the shrinkage of the neighbouring bars and so the effect on the structure's stiffness becomes secondary. For a hydrogel, the effect is considerably more noticeable, since the nodes do shrink in volume by a factor ϕ. This explains why the LCE is able to achieve larger shear moduli than the hydrogel.

Interestingly, the dependence of μ on the control parameter is qualitatively reproduced by a simplified system of point particles arranged in a periodic diamond lattice with nearest neighbour interaction given by Eqs. (14) and (16) for a LCE and a hydrogel, respectively. The fact that such a minimal model captures the essential features of the more complex FEM model indicates that

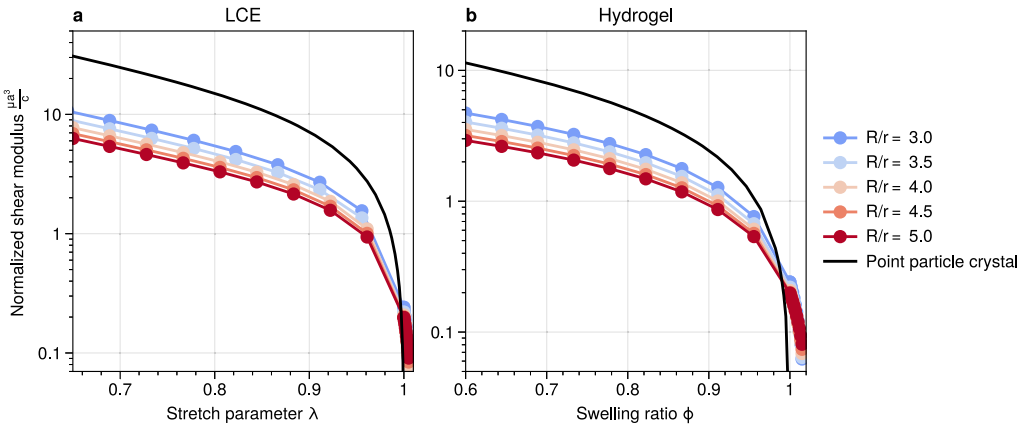

Fig. 5. Shear modulus of a 2x2x2 pentamode cube made of (a) a liquid crystal elastomer as a function of its stretch parameter λ and (b) an incompressible hydrogel as a function of its swelling ratio ϕ. In both cases, a drop in the shearing modulus is observed when the parameter crosses the threshold of $\lambda, \phi = 1$. For the case of the LCE, the decrease of at least three orders of magnitude is observed, whereas the decrease of the hydrogel is of two orders of magnitude. The black line corresponds to the shear modulus for a periodic diamond lattice of point particles with an nearest neighbour interaction function given by (a) Eq. (14) and (b) Eq. (16), computed with the aid of automatic differentiation package JAX. Such system, while much simpler, captures the qualitative behaviour observed in the FEM-simulations.

the tension build up due to geometric frustration, at the very least, plays a major role in the behaviour of the system's rigidity, notwithstanding intricate details such as the finite size of the nodes. The minimal model has the advantage of allowing analytical computation of the moduli, a fact that we now explore in greater detail.

3.2. Analytical modulus calculation from the band structure

We can take advantage of the piecewise ansatz in Eqs. (13) and (15) to analytically approximate the modulus corresponding to any imposed deformation since it reduces the problem to that of point particles in a diamond crystal with a pairwise interaction given by Eq. (14) for a LCE and Eq. (16) for a hydrogel. The analytical treatment for both constituents yields similar results that can be cast into a single expression with control parameter $\chi = \lambda$ or ϕ. The problem may be further simplified by assuming that a) the lattice is periodic and b) that all bars respond equally, so that $\beta_i = \beta_0 \forall i$. If the crystal is constrained to a fixed volume, then $\beta_0 = 1$ is a feasible guess, from which the hessian matrix can be computed. This approximate solution is well justified by the simulation results in Fig. 3, where displacement at the nodes is negligible. Since the pentamode is a periodic lattice with a crystal symmetry, the eigenvalue problem of the Hessian reduces to that of a dynamical matrix of a single lattice site with Fourier coefficients $D(\vec{q}, \chi)$ for some wave vector $\vec{q}$. For the particular case of a diamond, each lattice site has two nodes in three dimensions, so $D(\vec{q}, \chi)$ is a 6x6 matrix given by

$$\frac{L_0^2}{c} D(\vec{q}, \chi) = 4\epsilon_0(\chi) I_{6\times 6} + \begin{bmatrix} 0 & H_{ab}(\vec{q}, \chi) \\ H_{ab}^{\dagger}(\vec{q}, \chi) & 0 \end{bmatrix}, \tag{20}$$

where $L_0 = \sqrt{3}a/4$ is the unperturbed length of the crystal with lattice constant a, $\epsilon_0(\chi)$ is a prefactor and $H_{ab}(\vec{q}, \chi)$ are control parameter dependent off-diagonal 3×3 elements of the dynamical matrix. The corresponding expressions are given in Appendix D.

The eigenvalues ω^2 of the full $6N$ Hessian will then correspond to those of the dynamical matrix at wavevectors $\vec{q} = 2\pi(\frac{k_x}{N_x+1}, \frac{k_y}{N_y+1}, \frac{k_z}{N_z+1})$ with $0 \leq k_{x_i} \leq N_{x_i}$. The $6N$ dimensional eigenvectors will be given by $\vec{u}_{\vec{q}} = \{\hat{u} e^{i\langle \vec{q}, n^j \vec{a}_j \rangle}\}_{n_j \leq N_{x_j}}$ where $\hat{u}$ is the 6 dimensional polarization eigenvector of the dynamical matrix. The band diagram is reproduced in Fig. 6 for the case of a LCE , i.e. with Eq. (14) as edge energy function, by diagonalizing $D(\vec{q})$ with $N_{x_i} = 50$ for several values of the control parameter $\chi = \lambda$. Furthermore, we plot the corresponding density of states $g(\omega)$. It is worth noting that our calculation thus far is very similar to that by Takahashi et al. (2017), who considered a diamond lattice, but with Hookean springs.

The shear modulus can then be computed as the linear response to a shear force field along the $(-1, 1, 1)$ outermost planes, labelled $n_x = 0$ and $n_x = N_x$, parallel to the vector $\hat{a}_2 + \hat{a}_3$, so that $\hat{f} \propto (\hat{a}_2 + \hat{a}_3)(\delta_{n_x,0} - \delta_{n_x,N_x})$, as sketched in Fig. 6(c). We find that this probing field selects the transverse modes propagating along the wavevector $q_x(-1, 1, 1)$ with polarization parallel to $\hat{a}_2 + \hat{a}_3$. There are two such branches, an acoustic and an optical. Their dispersion relations read

$$\begin{aligned} \frac{3a^2}{16c}\omega_a^2 &= f(\chi)(1 - \cos q_x a) \,, \\ \frac{3a^2}{16c}\omega_o^2 &= \omega_0(\chi) + f(\chi)\cos q_x a \,, \end{aligned} \tag{21}$$

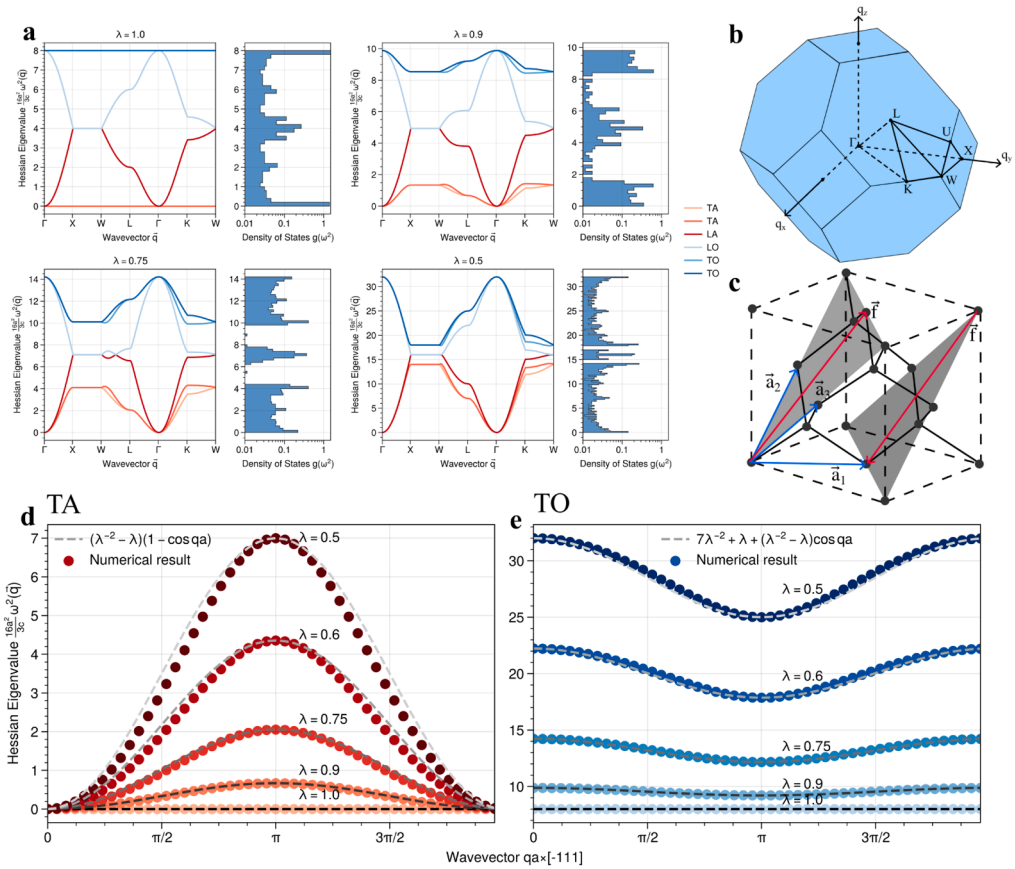

Fig. 6. (a) Band structure $\omega^2(\vec{q})$ of a periodic diamond lattice with nearest neighbour interaction given by Eq. (14) for different values of the stretch parameter $\chi = \lambda$, along with the corresponding density of states $g(\omega^2)$. The abbreviations on the legend stand for TA = Transverse Acoustic, LA = Longitudinal Acoustic, TO = Transverse Optical and LO = Longitudinal Optical. For a relaxed structure with $\lambda = 1$, the transverse acoustic modes are all zero modes and appear as two flat bands. The abundance of soft modes is captured in the sharp peak at $\omega^2 = 0$ in $g(\omega^2)$. As λ is decreased below unity, the tension in the edges eliminates all zero modes, thus lifting the transverse acoustic bands and broadening the peak in the density of states. Moreover, the transverse modes exhibit a gap that closes with decreasing λ, demonstrating that the stretch parameter can also tune the transverse band gap. (b) The first Brillouin zone of an FCC lattice with its high symmetry points X,W,U,L,K and Γ. (c) The shearing force protocol $\vec{f}$: the nodes in the two outermost (-1,1,1) planes of the crystal, shaded in gray, experience an in-plane force parallel to the vector $\vec{a}_2 + \vec{a}_3$, depicted in scarlet. The planes experience antiparallel forces so that mechanical balance is maintained. (d and e) Dispersion relation for (d) the transverse acoustic branch and (e) the transverse optical band, predicted by Eq. (21). The agreement between the prediction and the numerical diagonalization of Eq. (20) demonstrates the validity of Eq. (21).

where ω_a is the dispersion of the acoustic branch, ω_o is the dispersion of the optical branch, $f(\chi)$ are the mean field edge tensions and ω_0 is the minimum of the optical band. The latter two are constituent dependent, and are given by

$$f(\chi) = \begin{cases} \chi^{-2} - \chi & \text{(LCE)} \\ \chi^{-2/3}(1-\chi) & \text{(Hydrogel)} \end{cases}$$
$$\omega_0(\chi) = \begin{cases} 7\chi^{-2} + \chi & \text{(LCE)} \\ \chi^{-2/3}(7+\chi) & \text{(Hydrogel).} \end{cases} \tag{22}$$

The parameter f can be verified to be the mean field tension by computing $U'(\beta = 1)$. Details of the derivation of these expressions may be found in Appendix D.

Fig. 6(a) and Eq. (21) show that decreasing the control parameter χ below unity eliminates all of the zero modes; for a state with $\chi = 1$, the network has ample zero modes, as evinced by the two flat degenerate acoustic bands and the peak in the density of states at $\omega = 0$. This coincides with Eqs. (21) and (22), where the tension $f(\chi = 1) = 0$ and the acoustic dispersion ω_a flattens to 0. This means that $\mu(\chi = 1) = 0$ as the probe will have a non zero projection on the kernel of H. Lowering $\chi < 1$ induces a state of geometric frustration in which the zero modes now have a finite energy cost, so the bands are lifted and the peak in the density of states broadens. Furthermore, the more χ is reduced, the greater the energy cost of these modes. This demonstrates the phase velocity

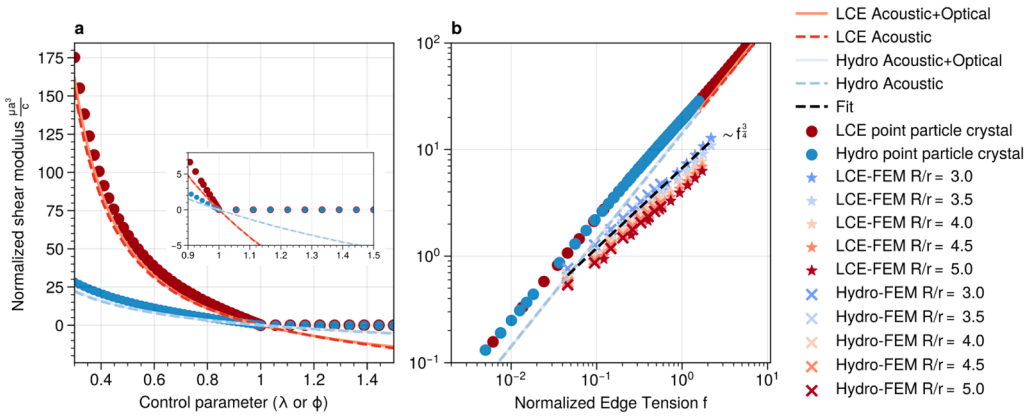

Fig. 7. (a) Shear modulus as a function of the control parameter λ or ϕ for point particles in a diamond crystal with nearest neighbour interaction given by Eq. (14) for a LCE, in red, and Eq. (16) for a hydrogel, in blue. The continuous curves represent the prediction of Eq. (23) without (labelled "Acoustic") and with (labelled "Acoustic + Optical") the contribution of optical modes. The points are simulation results for a cube of 10^3 unit cells, computed via Eq. (8) with the automatic differentiation package JAX. Good agreement is observed between the three sets for a control parameter below 1, validtaing Eq. (23) and demonstrating that optical modes are negligible. For a control parameter above unity, the system relaxes to a new state with zero modes, so μ stagnates at 0 and $\beta = 1$ is no longer a good approximation. (b) Shear modulus as a function of analytical edge tensions f given in Eq. (22) for the FEM simulations, the JAX simulations and the analytical prediction with and without optical mode contribution. All three exhibit a power law like scaling with different exponents; the shear modulus of the point particle crystal adequately follows the theoretical prediction of a scaling exponent of 1. In contrast, the FEM simulations show a scaling exponent of $\sim 3/4$, which stems from additional contributions such as the finite size of the nodes.

of transverse modes is controlled by the edge tension through the stretch parameter χ. Additionally, we observe that the transverse optical and acoustic bands come closer together for decreasing χ; the band gap of transverse modes can also be tuned through χ.

Eq. (21) deserves a comment; the acoustic dispersion relation near the Γ point is given by $\omega^2 \propto f(\chi) q_x^2 a^2$, from which it follows that the speed of sound is $v_s \propto a\sqrt{f(\chi)}$. The quadratic dispersion is seen in Fig. 6(a) and (d). Because $f(\chi)$ is the mean field edge tension, this equation is reminiscent of the wave speed for a string with tension T, $v_s \propto \sqrt{T}$. While the pentamode is usually referred to as a "metafluid", in light of this relation a more accurate description would be a three dimensional self tensing "metastring"; its transverse modes can be tuned by controlling the edge tension in the same way a string's dispersion relation is controlled by its tension per unit length. Additionally, its transverse modes are floppy for the case of no tension, in the same way string without tension can freely move in its transverse direction.

From Eq. (9) and the dispersion relation in Eq. (21), the shear modulus then reads

$$\mu = \frac{8c}{3a^3}\left(\frac{3}{16 f(\chi)} + \frac{I(\chi)}{16\omega_0}\right)^{-1} \approx \frac{128c}{9a^3} f(\chi), \tag{23}$$

where $I(\chi)$ is a function of the ratio $f(\chi)/\omega_0(\chi)$ given in Appendix D. The last approximation neglects the high frequency optical contribution.

This result is verified in Fig. 7(a) where it is plotted and compared to a numerical simulation of pointlike particles in a diamond lattice with nearest-neighbour interaction given by Eq. (14), in red, or Eq. (16), in blue. The modulus for such a system is numerically calculated using the definition in Eq. (8) and the automatic differentiation package JAX. Reasonable agreement between theory and simulation is observed in the overall dependence of the modulus on the control parameter and the edge tension in the regime of positive tension, which coincides with a control parameter below 1. The discrepancies between simulation and theory in this regime arise from deviations from our trial solution $\beta = 1$. For a control parameter above 1, the tension becomes negative and so does μ by Eq. (23), indicating an instability. This means that our solution $\beta = 1$ is no longer valid, and the system relaxes to a new state which still has floppy modes; for point particles with pairwise interactions, the vertices rearrange in a similar fashion to how a compressed string can bend in the transverse direction. For the system of an elastic continuous medium, this induces a buckling instability which cannot be captured by a piecewise constant ansatz such as that of Eqs. (13) and (15).

The diagonalization of the Hessian in Eq. (20) is exact for the case of point particle crystals with periodic boundary conditions, and therefore in this approximation all Bloch modes are propagating Bloch modes (i.e. $\vec{q} \in \mathbb{R}^3$). Nevertheless, this is not necessarily the case for continuous elastic systems and systems of finite size, where evanescent modes with $\vec{q} \in \mathbb{C}^3$ may be present (Chen et al., 2024). These modes are expected to contribute to the shear modulus for systems of finite size, which could partially explain the discrepancy between the point particle lattice and the FEM results. A more accurate calculation could include this modes by restricting the crystal to have a finite size. However, this comes at the expense of a Hessian which is no longer block circulant and thus considerably harder to diagonalize analytically. Alternatively, the band structure could be better approximated by numerically solving the eigenvalue problem for the harmonic incremental equations, which would inevitably require the usage of FEM.

Perhaps the most interesting prediction of Eq. (23) is the linear scaling with edge tension $f(\chi)$, a behaviour which can already be inferred from Eq. (A.2) and a mean field argument. We test the validity of such scaling for both the point particle system and the FEM model in Fig. 7(b), where the modulus is plotted against the analytical edge tension for positive edge tension. In all cases we observe a power law like scaling, as evinced by a straight line in a log-log plot. The point particle case adequately follows the theoretical scaling, with minor discrepancies for lower tensions due to deviations from the trial solution $\beta = 1$. This solution becomes asymptotically exact in the limit of large tension. For the case of the FEM model, we find that both constituents yield a similar scaling law with a critical exponent of $\sim 3/4$, not far from the exponent of 1 predicted by theory. This discrepancy arises mainly due to additional effects such as the elastic response of the finite sized nodes. Nevertheless, the power law scaling survives within the tested regime. In the future, smaller values of the control parameter could be simulated to test whether the scaling becomes asymptotically accurate for the FEM model as well, but this is a computationally challenging task due to the large deformations and contractions stemming from extreme actuation.

4. Discussion

Here we have proposed a new type of stimuli-responsive mechanical metamaterial, capable of dynamically switching between a floppy and a rigid state due to geometric incompatibility. Such a mechanical switch owes its properties to the generation of a frustrated state due to the incompatibility of the constituent's rest configuration and a fixed unit cell, akin to the geometric incompatibility predicted by disordered spring networks (Merkel et al., 2019) and vertex models (Hernandez et al., 2022), which are commonly used to model polymer networks and epithelial tissue, respectively. The suggested strategy to tune rigidity through geometric incompatibility complements earlier work on variable stiffness of multiphase metamaterial, in which one phase undergoes a material transition, in particular a melting transition (Zheng et al., 2024), a first order jamming transition (Wang et al., 2024) or a glass transition (Chen et al., 2022). We analytically estimated the moduli of our structures via a variational ansatz, which results a linear scaling with edge tension. This scaling is well verified by numerical computation of point particles in a lattice. The hyperelastic continuous model also shows a power law behavior, but with a different exponent of $\sim 3/4$. The relation of edge tension, stemming from geometric frustration, and the shear modulus illustrates the relationship between zero modes, or their absence, and the rigidity of the system.

We expect that a realization of our system is within the current reach of 3D printing technologies. LCE actuators based on photoresin inks containing the liquid crystal mixture E7 are capable of strains up to 20 % when heated to 180 ° C (Hsu et al., 2024; Münchinger et al., 2022). Such strains were achieved by optically heating and the response time of the structure was observed to be in the order of seconds (Münchinger et al., 2022). In our model, a strain of 20 % corresponds to $\lambda = 0.8$, and so according to Fig. 5, this would increase the modulus by over an order of magnitude. Furthermore, pNIPAM microprinted hydrogels have been found to shrink up to 45 % when heated to 70 ° C (Tran et al., 2025). A hydrogel realization would have the additional advantage of actuation via pH instead of temperature, and thus no external energy input would be required. Nevertheless, it is imperative that the hydrogel is tough enough to withstand the prestress (Hua et al., 2020). Since the pentamode has already been realized via two-photon laser printing with an unresponsive constituent (Kadic et al., 2012), it remains to fabricate it with a responsive medium and to fix its outer most nodes. We envision two possibilities for this: either glue the outer surfaces to externally fixed planes or join the nodes of opposing surfaces with rigid bars. We note that our blueprint has the practical advantages of simple fabrication due to the usage of a single constituent, low power actuation (especially in the case of pH-sensitive hydrogel) and the possibility of realizations at the micron scale.

An important aspect of our proposed control strategy is that it can continuously change the elastic modulus as a function of prestress, or, equivalently, of actuation strength. Consequently, it can access every value in between its span. This marks a stark contrast to solid-liquid transition based metamaterials, which can only discontinuously jump between two stiffness values. Such fine control is possible because the control parameter λ or ϕ can be tuned in a continuous fashion; for hydrogels, swelling occurs due to the osmotic pressure resulting from the dissociation of ionic groups, which can be controlled via concentration changes (Hua et al., 2020; Bayat et al., 2020). For LCEs, continuity in the generation of spontaneous strain comes from the quenched disorder induced by the polymeric matrix, which smoothens the first order phase transition of a pure liquid crystal and thus permits temperature dependent, continuously tunable strain (Münchinger et al., 2022; Petridis and Terentjev, 2006; Selinger et al., 2002).

Compared to jamming based control, an important strength of prestress based control is that theoretically no upper bound exists, as demonstrated by Eq. (23); the larger the tension, the larger the modulus. The true limit will be set by experimental parameters such as the ability to sustain the prestress without damage or the extent of possible actuation strength. Jamming, on the other hand, is limited by the coordination number; the modulus will stagnate at the jamming limit, where all possible contacts among neighbours have been realized, and thus any further actuation will not result in any stiffness increase.

Our theoretical approach models a purely elastic system with no viscous losses. This is sufficient in our context because we suggest the use of materials that are solid on large time scales. Rheology measurements on LCEs have shown that the low frequency loss modulus G'' is at least two orders of magnitude below the storage modulus G', a difference which increases with decreasing frequency (Martinoty et al., 2004). The situation is similar for tough hydrogels, which have been reported to have a storage modulus of 1–2 orders of magnitude larger than the loss modulus (Song et al., 2016; Ren et al., 2025).

The bulk of this work focuses on the regime of a control parameter below unity, in which the edge tension is always positive and the elastic body experiences extensile strain. While this is the regime of interest for the purpose of rigidfying a floppy system such as a pentamode, the effect of a compressive stress with a control parameter above unity poses an interesting perspective for further research; a growing constituent is expected to produce a buckling instability and so the modulus should respond discontinuously in a phase transition fashion, similar to the behaviour shown in Fig. 7(a) for point particles and reported elsewhere (Merkel et al., 2019).

In that sense, the proposed metamaterial could serve as a blueprint for a printable reversible mechanical transition. Simulating such symmetry breaking in a complex system like a pentamode within a FEM framework can be challenging, requiring complex algorithms such as deflation algorithms to describe the buckling bifurcation (Farrell et al., 2016).

Another possible direction of future work is to control the pre-stress of the constituent anisotropically in order to independently taylor the entries of the fourth order Cauchy moduli tensor C_{ijkl} via symmetry breaking. This could be achieved by using two constituents with a different response upon external stimuli, for example, a linear elastic material and a LCE elastomer. Some work in this direction has been proposed by Nguyen et al., where a phononic crystal composed of an elastic solid with responsive hyperelastic inclusions leads to a tunable bandgap due to breaking of inversion symmetry (Nguyen et al., 2019).

Finally, the crystal symmetries of the underlying lattice equip such a printable system with exciting possibilities of mechanical edge modes; as Takahashi et al. (2017) demonstrated for the case of Hookean springs, a mechanical realization of a diamond lattice with variable edge tension has nodal lines in its dispersion relation which are topologically protected by chiral symmetry. Some of these features are already observed in the band structure of a pentamode with a linear elastic material, where closure of the band gap along the XW direction is present, leading to protected nodal lines (Martin et al., 2012). In the case of point particles, the topological features of the zero edge modes can be tuned via the tension, which in our case is controlled via the parameter λ or ϕ. It remains to see how the tension affects the topological properties of the responsive pentamode with links of finite size. Thus, the proposed metamaterial is interesting beyond its tunable moduli, as it provides an experimentally realizable system of tunable topological edge modes.

CRediT authorship contribution statement

Santiago Gomez Melo: Writing – review & editing, Writing – original draft, Visualization, Validation, Software, Investigation, Formal analysis, Conceptualization; **Falko Ziebert:** Writing – review & editing, Validation, Supervision, Conceptualization; **Ulrich S. Schwarz:** Writing – review & editing, Validation, Supervision, Conceptualization, Resources.

Data availability

Our computer code is available at https://github.com/sgomezmelo/Dynamic-Rigidity-Control-MM.

Declaration of competing interest

The authors declare that they have no known competing financial interests or personal relationships that could have appeared to influence the work reported in this paper.

Acknowledgment

We thank Eva Blasco, Martin Wegener and Yi Chen for helpful discussions. This work was supported by the Deutsche Forschungsgemeinschaft (DFG, German Research Foundation) via the Cluster of Excellence “3D Matter Made to Order (3DMM2O)” (EXC-2082/1-390761711 and EXC-2082/2-390761711, to USS).

Appendix A. Prestress stability of an all tensed network

Here we prove the claim in the main text that a network with no disjoint subnetworks with all edges under tension will be prestress stable. We do so by restricting the P in Eq. (2) to the subspace of linear zero modes. The restricted operator reads

$$P = \frac{U'(L_\alpha)}{L_\alpha}\left(g_{\alpha i}g_{\alpha j}\delta_{\eta\kappa} - R_{\alpha i\eta}R_{\alpha j\kappa}\right) \implies P|_{\ker(R)} = \sum_\alpha \frac{U'(L_\alpha)}{L_\alpha} g_{\alpha i}g_{\alpha j}\delta_{\eta\kappa}, \tag{A.1}$$

and now we compute the inner product of any vector $\vec{v}$ and its image $P\vec{v}$, denoted by $\langle \vec{v}, P\vec{v}\rangle$,

$$\langle \vec{v}, P\vec{v}\rangle = \sum_{\alpha i j \eta} \frac{U'(L_\alpha)}{L_\alpha} \underbrace{(g_{\alpha i}v_{i\eta})(g_{\alpha j}v_{j\eta})}_{>0} > 0, \tag{A.2}$$

where in the last line we used the fact that a the kernel of g for a network with a single connected subgraph is one dimensional and spanned by the rigid motion $\vec{v}_1 = (1, 1, \dots, 1)$ (Godsil and Royle, 2013), so that for all non trivial zero modes $\vec{v} \notin \text{span}(\vec{v}_1) \implies g_{\alpha i}v_{i\eta} \neq \vec{0}$.

Appendix B. Elastic moduli of mechanical networks

The derivation of an expression from the definition of elastic moduli in Eq. (8) involving the eigenvalues lies within the framework of linear response; in the presence of a driving force field $f(t)$, an infinitesimal dynamic displacement around an equilibrium

configuration $\delta x(t)$ follows the equations of motion given by

$$\begin{aligned} m\delta\ddot{x}(t)_{i\eta} &= -\partial_{u_{i\eta}} E + f_{i\eta} = -\sum_{j\kappa} H_{i\eta j\kappa}\delta x(t)_{j\kappa} + f(t)_{i\eta} \\ \implies -m\omega^2\delta x_{i\eta}(\omega) &= -\sum_{j\kappa} H_{i\eta j\kappa}\delta x(\omega)_{j\kappa} + f(\omega)_{i\eta} \\ \implies f_{i\eta} &= \sum_{j\kappa}(H - m\omega^2 I)_{i\eta j\kappa}\delta x_{j\kappa}, \end{aligned} \tag{B.1}$$

where $f_{i\eta}$ is usually restricted to the boundaries of the network, and in the second line Newton's second law is Fourier-transformed. The system of equations in Eq. (B.1) becomes singular when $m\omega^2$ is an eigenvalue of the Hessian, thus producing a resonance. In particular, for the static limit, $\omega \to 0$, Eq. (B.1) becomes

$$f_{i\eta} = \sum_{j\kappa} H_{i\eta j\kappa}\delta x_{j\kappa}, \tag{B.2}$$

which is a force balance condition, i.e. the system counteracts the applied force in equilibrium. For underconstrained systems with linear zero modes, H is singular because $\omega = 0$ is an eigenvalue with a non-trivial associated subspace (i.e. not solely composed of rigid transformations). Therefore, this equation does not necessarily have a solution; there are forces that the system cannot counteract. In order for the system to be solvable, $f \in$Im(H). Since the $3N$ dimensional force vector space can be decomposed as a direct sum ker(H)$\oplus$Im(H), it follows that f must have zero projection on the space of zero modes. If $f \notin$Im(H) then we define the associated modulus to be $\mu = 0$ since the force cannot be counteracted. If, on the other hand, this solvability condition is met, then the work done W on the system can be written in terms of the orthonormal eigenbasis of H, $\hat{u}_i$,

$$\begin{aligned} W = \langle \vec{f}, \delta x\rangle &= \Big\langle \sum_i \langle \vec{f}, \hat{u}_i\rangle \hat{u}_i, \sum_j \langle \delta x, \hat{u}_j\rangle \hat{u}_j \Big\rangle \\ &= \Big\langle \sum_{i|\omega_i\neq 0} \langle \vec{f}, \hat{u}_i\rangle \hat{u}_i, \sum_j \langle \delta x, \hat{u}_j\rangle \hat{u}_j \Big\rangle \\ &= \sum_{i|\omega_i\neq 0} \langle \vec{f}, \hat{u}_i\rangle\langle \delta x, \hat{u}_i\rangle = \sum_{i|\omega_i\neq 0} \frac{\langle \vec{f}, \hat{u}_i\rangle^2}{\omega_i^2}, \end{aligned} \tag{B.3}$$

where in the last step we used Eq. (B.2) represented in the eigenbasis of H, i.e. $\langle f, \hat{u}_i\rangle = \omega_i^2\langle \delta x, \hat{u}_i\rangle$. The aforementioned calculation corrects that of Pessot et al. (2016) in order to account for the non-trivial kernel of H, so that the sum excludes the zero modes and the ω in the denominator does not become pathological. Additionally, we note that the squared norm of their unnormalized eigenbasis $\vec{u}_i$ will be proportional to the number of degrees of freedom in the system $|\vec{u}_i|^2 \propto N$. Consequently, this is an *intensive* energy change, i.e work per unit cell with volume a^3. From Eq. (B.3) the modulus μ associated to a particular probing force can be extracted by separating $\vec{f} = \sigma\hat{f}$ and differentiating twice per the definition in Eq. (8),

$$\mu = \begin{cases} 0 & \text{proj}_{\ker(H)} f \neq 0 \\ \frac{a^3}{2}\left(\sum_{k|\omega_k\neq 0} \frac{\langle \hat{u}_k, \hat{f}\rangle^2}{\omega_k^2}\right)^{-1} & \text{otherwise,} \end{cases} \tag{B.4}$$

where $\hat{f}$ is the normalized $3N$ dimensional vector associated with $\vec{f}$, which has magnitude σ.

Finally, we show that the eigenvalues, and by extension the modulus given in Eq. (9), are a non decreasing function of the tensions U'. Note that this cannot be deduced from positive definiteness alone since a positive eigenvalue could in principle decrease but still remain positive. We prove our claim by writing the eigenvalue as an inner product:

$$\omega_k^2 = \langle u_k, Hu_k\rangle = \sum_\alpha U''_\alpha \langle Ru_k, Ru_k\rangle + \langle u_k, Pu_k\rangle, \tag{B.5}$$

focusing on the prestress stability contribution,

$$\begin{aligned} \langle u, Pu\rangle &= \sum_{\alpha i\eta j\mu} \frac{U'(L_\alpha)}{L_\alpha}\Big(g_{\alpha i}g_{\alpha j}\delta_{\eta\kappa} - R_{\alpha i\eta}R_{\alpha j\kappa}\Big)u_{j\eta}u_{i\kappa} \\ &= \sum_\alpha \frac{U'(L_\alpha)}{L_\alpha}\Big(\sum_\eta v_{\alpha\eta}v_{\alpha\eta} - \sum_\eta \frac{L_{\alpha\mu}}{L_\alpha}v_{\alpha\mu}\sum_\eta \frac{L_{\alpha\mu}}{L_\alpha}v_{\alpha\mu}\Big), \end{aligned} \tag{B.6}$$

where we have abbreviated $v_{\alpha\mu} = \sum_i g_{\alpha i}u_{i\mu}$. The claim is true if the term in parenthesis is non-negative, a fact which follows from the Cauchy-Schwarz inequality

$$\begin{aligned} &\Big(\sum_\mu \frac{L_{\alpha\mu}}{L_\alpha}v_{\alpha\mu}\Big)\Big(\sum_\mu \frac{L_{\alpha\mu}}{L_\alpha}v_{\alpha\mu}\Big) \leq \Big(\sum_\mu \frac{L_{\alpha\mu}}{L_\alpha}\frac{L_{\alpha\mu}}{L_\alpha}\Big)\Big(\sum_\mu v_{\alpha\mu}v_{\alpha\mu}\Big) = \sum_\mu v_{\alpha\mu}v_{\alpha\mu} \\ \implies &\sum_\mu v_{\alpha\mu}v_{\alpha\mu} - \Big(\sum_\mu \frac{L_{\alpha\mu}}{L_\alpha}v_{\alpha\mu}\Big)\Big(\sum_\mu \frac{L_{\alpha\mu}}{L_\alpha}v_{\alpha\mu}\Big) \geq 0. \end{aligned} \tag{B.7}$$

Appendix C. Auxiliar strain measures

In the main text the strain measure of choice is the component of the Cauchy strain tensor C, defined in Eq. (19), along the axis of the bar $\hat{n}$. Here we report the standard Frobenius norm of the tensor $\sqrt{\mathrm{Tr}(C^T C)}$, also known as the equivalent or von Mises strain. Note that the definition of C in the main text is always deviatoric by construction. The equivalent strain is shown in Fig. C.8.

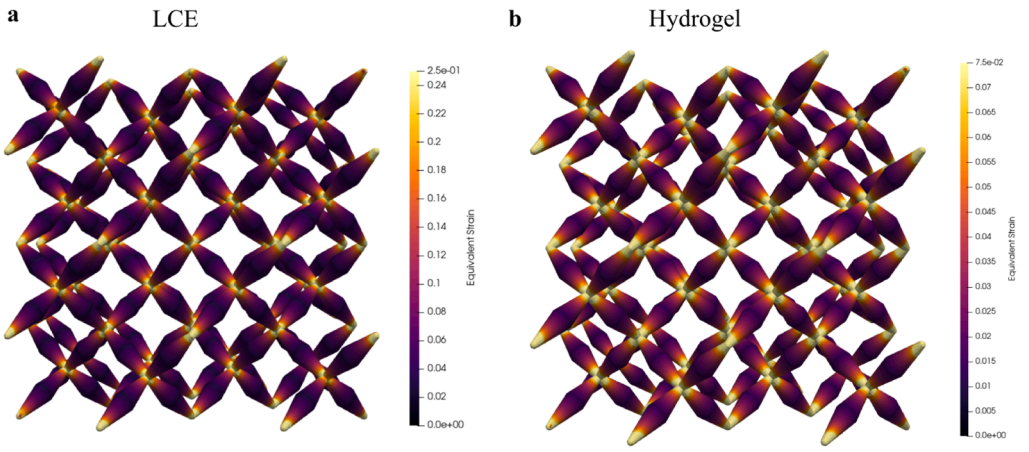

Fig. C.8. Equivalent Cauchy strain tensor, defined as the Frobenius norm of the Cauchy tensor defined in Eq. (19), for the case of a LCE with $\lambda = 0.9$(a) and a hydrogel with $\phi = 0.9$(b). In both cases the strain concentrates at the nodes, where the tension of the four adjacent bars must cancel in order to sustain mechanical equilibrium. In contrast, the center of the bars experience negligible strain.

The equivalent strain has an essentially identical spatial distribution as the component along the axis of the bar. Hence, the analysis remains the same.

Appendix D. Shear modulus of a prestressed diamond lattice

In this section we compute in detail the band stucture and linear response to shear from the spectrum of the dynamical matrix given in Eq. (20). The off diagonal elements of the dynamical matrix are given by

$$H_{ab}(\vec{q}) = -H_0 - \sum_{k=1}^{3} H_k e^{i\langle \vec{q}, \vec{a}_k \rangle}, \tag{D.1}$$

where $\vec{a}_k$ are the FCC lattice vectors $a_1 = a[0\ 1/2\ 1/2]$, $a_2 = a[1/2\ 0\ 1/2]$, $a_3 = a[1/2\ 1/2\ 0]$ and the matrix coefficients H_k are given by

$$\begin{aligned} H_0 &= \epsilon_1(\chi)\begin{bmatrix} \epsilon_2(\chi) & 1 & 1 \\ 1 & \epsilon_2(\chi) & 1 \\ 1 & 1 & \epsilon_2(\chi) \end{bmatrix}, H_1 = \epsilon_1(\chi)\begin{bmatrix} \epsilon_2(\chi) & -1 & -1 \\ -1 & \epsilon_2(\chi) & 1 \\ -1 & 1 & \epsilon_2(\chi) \end{bmatrix} \\ H_2 &= \epsilon_1(\chi)\begin{bmatrix} \epsilon_2(\chi) & -1 & 1 \\ -1 & \epsilon_2(\chi) & -1 \\ 1 & -1 & \epsilon_2(\chi) \end{bmatrix}, H_3 = \epsilon_1(\chi)\begin{bmatrix} \epsilon_2(\chi) & 1 & -1 \\ 1 & \epsilon_2(\chi) & -1 \\ -1 & -1 & \epsilon_2(\chi) \end{bmatrix}. \end{aligned} \tag{D.2}$$

where the parameters ϵ_1 and ϵ_2 are constituent dependent and given by

$$\epsilon_1 = \begin{cases} \lambda & \text{LCE} \\ \phi^{1/3} & \text{Hydrogel} \end{cases}, \epsilon_2 = \begin{cases} \lambda^{-3} & \text{LCE} \\ \phi^{-1} & \text{Hydrogel} \end{cases} \tag{D.3}$$

The prefactor ϵ_0 in Eq. (20) is given by $\epsilon_0 = \epsilon_1 \epsilon_2$.

In order to compute the modulus within the linear response regime, we define the following shearing force field:

$$\vec{f}_{\delta n^j} = \begin{cases} 0 & n^x \neq 0, N_z \text{ or } \delta = 1 \\ \frac{1}{4}\sqrt{\frac{3}{N_x N_y}}\sigma_0 a^2 \hat{v} & n^x = 0,\ \delta = 2 \\ -\frac{1}{4}\sqrt{\frac{3}{N_x N_y}}\sigma_0 a^2 \hat{v} & n^x = N_x,\ \delta = 2 \end{cases} \tag{D.4}$$

where $\delta = 1, 2$ labels the nodes in each lattice site, σ_0 is the intensity of the probing force per unit surface area and $\hat{v}$ is a unit vector in the direction of $\vec{a}_2 + \vec{a}_3$. The first condition requires that only the outermost planes spanned by the lattice vectors $\vec{a}_2$ and $\vec{a}_3$ experience a non-zero force, and that only one of the two nodes (labelled "2") experiences this force. The second and third condition impose

a constant force parallel to these planes, and opposite to each other so that the net external force on the whole crystal is 0. The prefactor $1/4\sqrt{3/N_xN_y}$ takes into account that the surface density of the sheared plane is $4/a^2\sqrt{3}$ atoms, and ensures normalization of the vector $\vec{f}/\sigma_0 a^2$. This force protocol is sketched in Fig. 6(c).

It then follows that the dot product with a generic eigenvector is:

$$\begin{aligned}\langle \vec{f}, \vec{u}_{\vec{q}}\rangle &= \sum_{n^j} \langle f_{\{n^j\}}, \hat{u}\rangle e^{i\langle \vec{q}, n^j \vec{a}_j\rangle} \\ &= \sum_{(n^x,n^y)} \frac{\sqrt{3}\sigma_0 a^2 \langle \hat{v}, \hat{u}\rangle}{4\sqrt{N_xN_y}} (1 - e^{iq_xN_xa}) e^{2\pi i(\frac{n^y}{N_y}q_y + \frac{n^z}{N_z}q_z)} \\ &= \frac{\sigma_0 a^2 \sqrt{3N_xN_y}}{4} \langle \hat{v}, \hat{u}\rangle (1 - e^{-iq_xa}) \delta_{q_z,0}\delta_{q_y,0},\end{aligned} \tag{D.5}$$

where we have used the geometric series identity and the fact that $e^{iq_xN_xa} = e^{-iq_xa}$ The dot product selects the direction along the first reciprocal vector $\vec{b}_1 = (-1,1,1)$ in k space; the contribution of all other modes to the work done is zero. Furthermore, the term $\langle \hat{v}, \hat{u}\rangle$ selects a particular polarization. Because $\vec{a}_2 + \vec{a}_3$ is perpendicular to $\vec{b}_3$, only transverse modes are excited; there will be an acoustic contribution and an optical contribution. It inmediately follows that if $\chi = 1$, $\vec{f}$ overlaps with the transverse acoustic zero modes, and so $\mu = 0$.

To compute the modulus in the case $\chi < 1$, analytical expressions for the transverse acoustic and transverse optical dispersion relation along the direction $\vec{b}_1$ are required. They can be obtained by restricting the matrix onto the associated subspace, which will result in a manageable 2x2 operator. These spaces will be spanned by vectors of the form $[1\ \pm 1] \otimes \hat{e}_i$, where $\hat{e}_i$ span the orthogonal compliment of $\vec{b}_1$. These vectors are

$$\begin{aligned} v_1^{\pm} &= \begin{bmatrix}1\\ \pm 1\end{bmatrix} \otimes (\vec{a}_2 + \vec{a}_3) = \begin{bmatrix}2\,1\,1 & \pm 2 & \pm 1 & \pm 1\end{bmatrix} \\ v_2^{\pm} &= \begin{bmatrix}1\\ \pm 1\end{bmatrix} \otimes (\vec{a}_2 - \vec{a}_3) = \begin{bmatrix}0\,-1\,1\,0 & \mp 1 & \pm 1\end{bmatrix},\end{aligned} \tag{D.6}$$

where the $+$ vectors correspond to acoustic modes and the $-$ vectors to optical modes. These vectors allow us to define restriction operators $Q^{\pm} = [v_1^{\pm}/|v_1^{\pm}|,\ v_2^{\pm}/|v_2^{\pm}|]$, from which the restriction of $D(q_z)$ onto the subspace is given by $D(q,\chi)|_{\mathrm{span}(v_1^{\pm}\ v_2^{\pm})} = QD(q,\chi)Q^{\dagger}$. Therefore, the restriction of $H(q_z)$ to the subspace of acoustic modes $\mathrm{span}(v_1^{+}\ v_2^{+})$ reads

$$\frac{3a^2}{16c} D(q,\chi)|_{\mathrm{span}(v_1^{+}\ v_2^{+})} = \underbrace{\overbrace{(\epsilon_1\epsilon_2 - \epsilon_1)}^{f(\chi)}(1 - \cos q_xa)}_{\omega_a^2(q)} I_{2\times 2}, \tag{D.7}$$

where the expression $f(\chi) = \epsilon_1\epsilon_2 - \epsilon_1$, which is the mean field tension in Eq. (22) in the main text, arose naturally. Since this restriction is diagonal, the dispersion relation of acoustic bands $\omega_a^2(q)$ are then given by the prefactor in Eq. (D.7). Note that this band flattens to 0 when $\chi = 1$, confirming that these modes are in the kernel of H and so $\mu(\chi = 1) = 0$. Similarly, the restriction onto the subspace of optical modes $\mathrm{span}(v_1^{-}\ v_2^{-})$ leads to a dispersion relation given by

$$\frac{3a^2}{16c}\omega_o^2(q) = \underbrace{7\epsilon_1\epsilon_2 + \epsilon_1}_{\omega_0(\chi)} + f(\chi)\cos q_xa = \omega_0(1 + b(\chi)\cos q_xa), \tag{D.8}$$

where the abbreviation $b(\chi) = f(\chi)/\omega_0(\chi)$ is used and $\omega_0(\chi)$ is the bottom of the optical band in Eq. (22) in the main text. These expressions are numerically verified in Fig. 6(d) and (e), where they are compared to the results of numerically diagonalizing the dynamical matrix for different values of qa.

From the analytical expression of the bands in Eqs. (D.7) and (D.8), and the dot product $\langle \vec{f}, \vec{u}_{\vec{q}}\rangle$ in Eq. (D.4), the modulus from Eq. (9) then reads

$$\frac{1}{\mu} = \frac{3}{8aN_lc}\sum_{q_x}\left(\frac{|\langle \hat{f}, \vec{u}_q^a\rangle|^2}{\omega_a^2(q)} + \frac{|\langle \hat{f}, \vec{u}_q^o\rangle|^2}{\omega_o^2(q)}\right), \tag{D.9}$$

where the factor $N_l = N_xN_yN_z$ comes from the normalization of $\vec{u}_q$. Since Eq. (D.9) essentially states that μ is a weighted harmonic mean over all eigenvalues, the optical contribution is negligible. We can nonetheless still derive an expression involving the two branches. We treat these two contributions separately; for the acoustic modes,

$$\begin{aligned}\sum_{q_x}\frac{|\langle \hat{f}, \vec{u}_q^a\rangle|^2}{\omega_a^2(q)} &= \frac{3N_xN_y|\langle \hat{v}, \vec{v}_q^a\rangle|^2a^4}{16f(\chi)}\sum_{q_x}\frac{|1 - e^{-iq_xa}|^2}{1 - \cos q_xa} \\ &= \frac{3N_xN_ya^4}{32f(\chi)}\sum_{q_x}\frac{2 - 2\cos q_xa}{1 - \cos q_xa} = \frac{3N_xN_yN_za^4}{16f(\chi)}.\end{aligned} \tag{D.10}$$

The optical mode contribution cannot be easily cast into a simple expression, so it is instead approximated by taking $N_z \to \infty$, which results in an integral,

$$\begin{aligned}\sum_{q_x} \frac{|\langle \hat{f}, \vec{u}_q^o \rangle|^2}{\omega_o^2(q)} &= \frac{3N_x N_y |\langle \hat{v}, \vec{v}_q^o \rangle|^2 a^4}{16\omega_0} \sum_{q_x} \frac{2 - 2\cos q_x a}{1 + b(\chi)\cos q_x a} \\ &\approx \frac{N_x N_y N_z a^4}{32\pi\omega_0} \int_0^{2\pi} \frac{1 - \cos x}{1 + b(\chi)\cos x} dx \\ &= \frac{N_x N_y N_z a^4}{16\omega_0} \underbrace{\left(\frac{\sqrt{b^{-2}(\chi) - 1}}{1 - b(\chi)} - \frac{1}{b(\chi)} \right)}_{I(\chi)}.\end{aligned} \tag{D.11}$$

One can check that $1/7 > b(\chi) > 0$ as long as the tension $f(\chi) > 0$ and that $\lim_{\chi \to 1^-} I(\chi) = \lim_{b \to 0^+} I(b) = 1$ so this expression is always well defined. Inserting Eqs. (D.10) and (D.11) into Eq. (D.9) yields Eq. (23) in the main text.

References

Aharoni, H., Xia, Y., Zhang, X., Kamien, R.D., Yang, S., 2018. Universal inverse design of surfaces with thin nematic elastomer sheets. Proc. Natl. Acad. Sci. 115 (28), 7206–7211. https://doi.org/10.1073/pnas.1804702115

Appiah, C., Arndt, C., Siemsen, K., Heitmann, A., Staubitz, A., Selhuber-Unkel, C., 2019. Living materials herald a new era in soft robotics. Adv. Mater. 31 (36). https://doi.org/10.1002/adma.201807747

Banerjee, S., Gardel, M.L., Schwarz, U.S., 2020. The actin cytoskeleton as an active adaptive material. Annu. Rev. Condens. Matter Phys. 11 (1), 421–439. https://doi.org/10.1146/annurev-conmatphys-031218-013231

Baratta, I.A., Dean, J.P., Dokken, J.S., Habera, M., Hale, J.S., Richardson, C.N., Rognes, M.E., Scroggs, M.W., Sime, N., Wells, G.N., 2023. DOLFINx: The Next Generation Fenics Problem Solving Environment. Zenodo. https://doi.org/10.5281/ZENODO.10447665

Bayat, M.R., Wang, K., Baghani, M., 2020. Visco-hyperelastic swelling and mechanical behavior of tough ph-sensitive hydrogels: theory development and numerical implementation. Int. J. Eng. Sci. 152, 103294. https://doi.org/10.1016/j.ijengsci.2020.103294

Calladine, C., 1978. Buckminster fuller's "tensegrity" structures and clerk Maxwell's rules for the construction of stiff frames. Int. J. Solids Struct. 14 (2), 161–172. https://doi.org/10.1016/0020-7683(78)90052-5

Chen, L., Zhao, C., Huang, J., Zhou, J., Liu, M., 2022. Enormous-stiffness-changing polymer networks by glass transition mediated microphase separation. Nat. Commun. 13 (1), 6941. https://doi.org/10.1038/s41467-022-34677-9

Chen, Y., Schneider, J. L.G., Wang, K., Scott, P., Kalt, S., Kadic, M., Wegener, M., 2024. Anomalous frozen evanescent phonons. Nat. Commun. 15 (1). https://doi.org/10.1038/s41467-024-52956-5

Chen, Y., Wang, K., Kadic, M., Guenneau, S., Wang, C., Wegener, M., 2023. Phonon transmission through a nonlocal metamaterial slab. Commun. Phys. 6 (1). https://doi.org/10.1038/s42005-023-01184-2

Connelly, R., Servatius, H., 1994. Higher-order rigidity—what is the proper definition? Discrete Comput. Geom. 11 (2), 193–200. https://doi.org/10.1007/bf02574003

Endresen, K., Murali, A., Serra, F., 2024. Actuation of cell sheets in 3D. https://doi.org/10.48550/ARXIV.2411.17834

Farhadifar, R., Röper, J.-C., Aigouy, B., Eaton, S., Jülicher, F., 2007. The influence of cell mechanics, cell-cell interactions, and proliferation on epithelial packing. Curr. Biol. 17 (24), 2095–2104. https://doi.org/10.1016/j.cub.2007.11.049

Farrell, P.E., Beentjes, C. H.L., Birkisson, A., 2016. The computation of disconnected bifurcation diagrams. https://doi.org/10.48550/ARXIV.1603.00809

Fuhrmann, J.F., Krishna, A., Paijmans, J., Duclut, C., Cwikla, G., Eaton, S., Popović, M., Jülicher, F., Modes, C.D., Dye, N.A., 2024. Active shape programming drives drosophila wing disc eversion. Sci. Adv. 10 (32). https://doi.org/10.1126/sciadv.adp0860

Godsil, C.D., Royle, G.F., 2013. Algebraic Graph Theory. Springer London, Limited.

Gomez Melo, S., Wörthmüller, D., Gönczy, P., Banterle, N., Schwarz, U.S., 2023. Grand canonical brownian dynamics simulations of adsorption and self-assembly of sas-6 rings on a surface. J. Chem. Phys. 158 (8). https://doi.org/10.1063/5.0135349

Goriely, A., 2017. The Mathematics and Mechanics of Biological Growth. Springer New York, New York, NY.

Gortler, S.J., Holmes-Cerfon, M., Theran, L., 2025. Higher order rigidity and energy. https://doi.org/10.48550/ARXIV.2506.03108

Hain, T., Santangelo, C., Manning, M.L., 2025. Optimizing properties on the critical rigidity manifold of underconstrained central-force networks. Phys. Rev. E 111 (1), 015418. https://doi.org/10.1103/physreve.111.015418

Hernandez, A., Staddon, M.F., Bowick, M.J., Marchetti, M.C., Moshe, M., 2022. Anomalous elasticity of a cellular tissue vertex model. Phys. Rev. E 105 (6), 064611. https://doi.org/10.1103/physreve.105.064611

Hsu, L.-Y., Melo, S.G., Vazquez-Martel, C., Spiegel, C.A., Ziebert, F., Schwarz, U.S., Blasco, E., 2024. Alignment and actuation of liquid crystals via 3D confinement and two-photon laser printing. Sci. Adv. 10 (36). https://doi.org/10.1126/sciadv.adq2597

Hua, M., Wu, D., Wu, S., Ma, Y., Alsaid, Y., He, X., 2020. 4D printable tough and thermoresponsive hydrogels. ACS Appl. Mater. Interfaces 13 (11), 12689–12697. https://doi.org/10.1021/acsami.0c17532

Kaczmarski, B., Leanza, S., Zhao, R., Kuhl, E., Moulton, D.E., Goriely, A., 2024. Minimal design of the elephant trunk as an active filament. Phys. Rev. Lett. 132 (24), 248402. https://doi.org/10.1103/physrevlett.132.248402

Kadic, M., Bückmann, T., Stenger, N., Thiel, M., Wegener, M., 2012. On the practicability of pentamode mechanical metamaterials. Appl. Phys. Lett. 100 (19). https://doi.org/10.1063/1.4709436

Kadic, M., Milton, G.W., van Hecke, M., Wegener, M., 2019. 3D metamaterials. Nat. Rev. Phys. 1 (3), 198–210. https://doi.org/10.1038/s42254-018-0018-y

Kane, C.L., Lubensky, T.C., 2013. Topological boundary modes in isostatic lattices. Nat. Phys. 10 (1), 39–45. https://doi.org/10.1038/nphys2835

Klein, H. C.R., Schwarz, U.S., 2014. Studying protein assembly with reversible brownian dynamics of patchy particles. J. Chem. Phys. 140 (18). https://doi.org/10.1063/1.4873708

Marée, A. F.M., Grieneisen, V.A., Edelstein-Keshet, L., 2012. How cells integrate complex stimuli: the effect of feedback from phosphoinositides and cell shape on cell polarization and motility. PLoS Comput. Biol. 8 (3), e1002402. https://doi.org/10.1371/journal.pcbi.1002402

Martin, A., Kadic, M., Schittny, R., Bückmann, T., Wegener, M., 2012. Phonon band structures of three-dimensional pentamode metamaterials. Phys. Rev. B 86 (15), 155116. https://doi.org/10.1103/physrevb.86.155116

Martinoty, P., Stein, P., Finkelmann, H., Pleiner, H., Brand, H.R., 2004. Mechanical properties of mono-domain side chain nematic elastomers. Eur. Phys. J. E 14 (4), 311–321. https://doi.org/10.1140/epje/i2003-10154-y

Maxwell, J.C., 1864. On the calculation of the equilibrium and stiffness of frames. Lond. Edinb. Dublin Philos. Mag. J. Sci. 27 (182), 294–299. https://doi.org/10.1080/14786446408643668

Merkel, M., Baumgarten, K., Tighe, B.P., Manning, M.L., 2019. A Minimal-Length Approach Unifies Rigidity in Underconstrained Materials. Vol. 116. National Acad Sciences. https://doi.org/10.1073/pnas.1815436116

Mihai, L.A., Goriely, A., 2021. Instabilities in liquid crystal elastomers. MRS Bull. 46 (9), 784–794. https://doi.org/10.1557/s43577-021-00115-2

Milton, G.W., Cherkaev, A.V., 1995. Which elasticity tensors are realizable? J. Eng. Mater. Technol. 117 (4), 483–493. https://doi.org/10.1115/1.2804743

Momeni, F., Hassani.N, S.M., Liu, X., Ni, J., 2017. A review of 4D printing. Mater. Des. 122, 42–79. https://doi.org/10.1016/j.matdes.2017.02.068
Münchinger, A., Hahn, V., Beutel, D., Woska, S., Monti, J., Rockstuhl, C., Blasco, E., Wegener, M., 2021. Multi-photon 4D printing of complex liquid crystalline microstructures by in situ alignment using electric fields. Adv. Mater. Technol. 7 (1). https://doi.org/10.1002/admt.202100944
Münchinger, A., Hsu, L.-Y., Fürniß, F., Blasco, E., Wegener, M., 2022. 3D optomechanical metamaterials. Mater. Today 59, 9–17. https://doi.org/10.1016/j.mattod.2022.08.020
Nguyen, B.H., Zhuang, X., Park, H.S., Rabczuk, T., 2019. Tunable topological bandgaps and frequencies in a pre-stressed soft phononic crystal. J. Appl. Phys. 125 (9). https://doi.org/10.1063/1.5066088
Nicolaou, Z.G., Motter, A.E., 2012. Mechanical metamaterials with negative compressibility transitions. Nat. Mater. 11 (7), 608–613. https://doi.org/10.1038/nmat3331
Peña, O. A., Martin, P., 2024. Cellular and molecular mechanisms of skin wound healing. Nat. Rev. Mol. Cell Biol. 25 (8), 599–616. https://doi.org/10.1038/s41580-024-00715-1
Pessot, G., Löwen, H., Menzel, A.M., 2016. Dynamic elastic moduli in magnetic gels: normal modes and linear response. J. Chem. Phys. 145 (10). https://doi.org/10.1063/1.4962365
Petridis, L., Terentjev, E.M., 2006. Nematic-isotropic transition with quenched disorder. Phys. Rev. E 74 (5), 051707. https://doi.org/10.1103/physreve.74.051707
Petridou, N.I., Corominas-Murtra, B., Heisenberg, C.-P., Hannezo, E., 2021. Rigidity percolation uncovers a structural basis for embryonic tissue phase transitions. Cell 184 (7), 1914–1928. e19. https://doi.org/10.1016/j.cell.2021.02.017
Ren, L., Shi, J., Liu, S., Wang, Z., Qiao, S., Weitz, D.A., Zhang, L., 2025. Tough hybrid hydrogels with exceptional swollen-state mechanical robustness via nanocrystalline domain engineering. Macromolecules 58 (15), 7975–7985. https://doi.org/10.1021/acs.macromol.5c00756
Rich, S., Jang, S., Park, Y., Majidi, C., 2017. Liquid metal-conductive thermoplastic elastomer integration for low-voltage stiffness tuning. Adv. Mater. Technol. 2 (12). https://doi.org/10.1002/admt.201700179
Scheibner, C., Souslov, A., Banerjee, D., Surówka, P., Irvine, W. T.M., Vitelli, V., 2020. Odd elasticity. Nat. Phys. 16 (4), 475–480. https://doi.org/10.1038/s41567-020-0795-y
Schwarz, U.S., Gompper, G., 1999. Systematic approach to bicontinuous cubic phases in ternary amphiphilic systems. Phys. Rev. E 59 (5), 5528.
Selinger, J.V., Jeon, H.G., Ratna, B.R., 2002. Isotropic-nematic transition in liquid-crystalline elastomers. Phys. Rev. Lett. 89 (22), 225701. https://doi.org/10.1103/physrevlett.89.225701
Sirote-Katz, C., Shohat, D., Merrigan, C., Lahini, Y., Nisoli, C., Shokef, Y., 2024. Emergent disorder and mechanical memory in periodic metamaterials. Nat. Commun. 15 (1). https://doi.org/10.1038/s41467-024-47780-w
Song, G., Zhao, Z., Peng, X., He, C., Weiss, R.A., Wang, H., 2016. Rheological behavior of tough PVP-in situ-PAAm hydrogels physically cross-linked by cooperative hydrogen bonding. Macromolecules 49 (21), 8265–8273. https://doi.org/10.1021/acs.macromol.6b01448
Takahashi, Y., Kariyado, T., Hatsugai, Y., 2017. Edge states of mechanical diamond and its topological origin. New J. Phys. 19 (3), 035003. https://doi.org/10.1088/1367-2630/aa5edb
Tran, H. B.D., Spiegel, C.A., Blasco, E., 2025. 4D printing of thermoresponsive oegma-based hydrogels with tunable response. Macromol. Mater. Eng. 310 (9), 202500096. https://doi.org/10.1002/mame.202500096
van Mastrigt, R., Dijkstra, M., van Hecke, M., Coulais, C., 2022. Machine learning of implicit combinatorial rules in mechanical metamaterials. Phys. Rev. Lett. 129 (19), 198003. https://doi.org/10.1103/physrevlett.129.198003
Wang, L., Xu, L., Wang, Z., Ye, L., Liu, Z., 2025. Design and Analysis of Variable Stiffness Continuum Actuator Based on Layer Jamming Principle. Springer Nature Singapore. pp. 803–818. https://doi.org/10.1007/978-981-96-1467-7_53
Wang, R., Cheng, C., Wang, H., Wang, D., 2024. Swollen hydrogel nanotechnology: advanced applications of the rudimentary swelling properties of hydrogels. ChemPhysMater 3 (4), 357–375. https://doi.org/10.1016/j.chphma.2024.07.006
Wang, Y., Li, L., Hofmann, D., Andrade, J.E., Daraio, C., 2021. Structured fabrics with tunable mechanical properties. Nature 596 (7871), 238–243. https://doi.org/10.1038/s41586-021-03698-7
Wang, Y., Ramirez, B., Carpenter, K., Naify, C., Hofmann, D.C., Daraio, C., 2019. Architected lattices with adaptive energy absorption. Extreme Mech. Lett. 33, 100557. https://doi.org/10.1016/j.eml.2019.100557
Warner, M., Terentjev, E. (Eds.), 2007. Liquid Crystal Elastomers. Number 120 In International series of monographs on physics, Clarendon Press, Oxford. rev. ed. edition. Includes liographical references (p. 382–392) and indexes. - Description based on print version record.
Webber, J.J., Worster, M.G., 2023. A linear-elastic-nonlinear-swelling theory for hydrogels. part 1. modelling of super-absorbent gels. J. Fluid Mech. 960. https://doi.org/10.1017/jfm.2023.200
Weichsel, J., Schwarz, U.S., 2010. Two competing orientation patterns explain experimentally observed anomalies in growing actin networks. Proc. Natl. Acad. Sci. 107 (14), 6304–6309. https://doi.org/10.1073/pnas.0913730107
Wool, R.P., 2008. Self-healing materials: a review. Soft Matter 4 (3), 400. https://doi.org/10.1039/b711716g
Yuen, M.C., Bilodeau, R.A., Kramer, R.K., 2016. Active variable stiffness fibers for multifunctional robotic fabrics. IEEE Robot. Autom. Lett. 1 (2), 708–715. https://doi.org/10.1109/lra.2016.2519609
Zheng, X., Watanabe, I., Wang, S., Chen, T.-T., Naito, M., 2024. Minimal-surface-based multiphase metamaterials with highly variable stiffness. Mater. Des. 237, 112548. https://doi.org/10.1016/j.matdes.2023.112548
Zheng, X., Zhang, X., Chen, T.-T., Watanabe, I., 2023. Deep learning in mechanical metamaterials: from prediction and generation to inverse design. Adv. Mater. 35 (45), 2302530.